Characterization of a cellulose acetate-based monophasic hybrid membrane in a single hemodialysis membrane module for blood purification

Adriana Gonçalves Janeca

Thesis to obtain the Master of Science Degree in

Biological Engineering

Supervisors:

Dr. Mónica Cristina Faria Besteiro

Prof. Dr. Maria Clara Henriques Baptista Gonçalves

Examination Committee

Chairperson: Prof. Dr. Duarte Miguel de França Teixeira dos Prazeres

Supervisor: Dr. Mónica Cristina Faria Besteiro

Member of the Committee: Prof. Dr. Marília Clemente Velez Mateus

October 2021

Preface

The work presented in this thesis was performed in the Department of Chemical Engineering of Instituto Superior Técnico (IST), University of Lisbon (Lisbon, Portugal). The work was performed as part of an ongoing project dedicated to the design of membrane module devices for artificial organs - one of the main research areas of the Center of Physics and Engineering of Advanced Materials (CeFEMA). CeFEMA is a Research Unit of IST dedicated to interdisciplinary research and education in physics, materials science, and engineering, emphasizing a thorough understanding of the underlying physical principles promoting materials design, processing, and characterization.

Research studies were performed during the period February-October 2021, under the supervision of Mónica Cristina Faria Besteiro (CeFEMA) and Maria Clara Henriques Baptista Gonçalves.

I declare that this document is an original work of my own authorship and that it fulfils all the requirements of the Code of Conduct and Good Practices of the Universidade de Lisboa.

Acknowledgments

The writing of this thesis could not have been successfully concluded, had it not been for the presence and contribution of crucial elements to whom I express my deepest gratitude.

To Dr. Mónica Faria, for the thorough guidance, countless hours towards enlightenment and energy funnelled into this project. For having believed in me when I thought I couldn’t.

To Prof. Clara Gonçalves, for the deepest insights, guidance, and crucial words of motivation. For never failing to explain the most inextricable subjects.

To all the colleagues in the laboratory, but mainly Flávia, who had been by my side since the day we cast our very first membrane, who always had the right words at the right times. For her inexhaustible patience and eagerness in assistance.

To my friends Vítor, Mariana, João, Rita, Daniel, Carolina, Joana and Ricardos, for their utmost support, encouragement, and reliability. For the heartfelt memories and never failing to lend a hand when weakness tried to prevail. May we keep holding onto each other for years to come.

To my parents for their unconditional love and emotional support. For teaching me the values of responsibility and resilience, transmitting their strength and faith, for being my first and oldest friendship.

To my grandparents, those in this and other worlds, for their kindness, wisdom, and love.

Abstract

A novel cellulose acetate-based monophasic hybrid skinned amine-functionalized CA-SiO_2-$(CH_2)_3NH_2$ membrane was synthesized by an innovative method which combines the phase inversion and sol-gel techniques.

The morphological characterization was performed by Scanning Electron Microscopy (SEM), and the chemical composition was analyzed by Fourier Transform Infrared Spectroscopy in Attenuated Total Reflection mode (ATR-FTIR). The characterization of the monophasic hybrid CA-SiO_2-$(CH_2)_3NH_2$ membrane in terms of permeation properties was carried out in an in-house built single hemodialysis membrane module (SHDMM) under dynamic conditions. Permeation experiments were performed to determine the hydraulic permeability (L_P), molecular weight cut-off (MWCO) and the rejection coefficients to urea, creatinine, uric acid, and albumin.

SEM confirmed the existence of a very thin (< 1 µm) top dense layer and a much thicker bottom porous surface, and ATR-FTIR showed the main bands belonging to CA based membranes. Permeation studies reveal that the L_P and MWCO of the CA-SiO_2-$(CH_2)_3NH_2$ membrane is 89.40 $mL.h^{-1}.m^{-2}.mmHg^{-1}$ and 24.5 kDa, respectively, and that the L_P is 1.8 times higher when compared to a pristine cellulose acetate membrane. Furthermore, the CA-SiO_2-$(CH_2)_3NH_2$ membrane fully permeates urea, creatinine, and uric acid while completely retaining albumin. Long-term filtration studies of albumin solutions indicate that fouling does not occur at the surface of the CA-SiO_2-$(CH_2)_3NH_2$ membrane.

Keywords: monophasic hybrid membrane; sol-gel; phase inversion; blood purification; ultrafiltration; cross-flow filtration; convection; hemodialysis

Resumo

Uma nova membrana híbrida monofásica, baseada em acetato de celulose e funcionalizada com grupos amina, CA-SiO_2-$(CH_2)_3NH_2$, foi sintetizada através de um método inovador que combinas as técnicas de inversão de fases e de sol-gel.

A caracterização morfológica da membrana foi conseguida através de *Scanning Electron Microscopy* (SEM) e respetiva composição química foi analisada através da técnica de espetroscopia *Attenuated Total Reflection - Fourier Transform Infrared* (ATR-FTIR). A caracterização da membrana híbrida monofásica CA-SiO_2-$(CH_2)_3NH_2$, em termos de propriedades de permeação, foi levada a cabo em condições dinâmicas, num módulo de hemodiálise de membrana única (SHDMM), previamente desenhado e projetado pelo laboratório. Os ensaios de permeação visaram a obtenção de parâmetros como a permeabilidade hidráulica (L_P), o valor de *cut-off* (MWCO) e os coeficientes de rejeição à ureia, creatinina, ácido úrico e albumina.

A análise SEM à membrana confirmou a presença de uma camada densa e fina (< 1 µm), adjacente a uma estrutura porosa, de espessura superior. A técnica de ATR-FTIR revelou a presença das principais bandas correspondentes a membranas baseadas em acetato de celulose. Os ensaios de permeação da membrana híbrida CA-SiO_2-$(CH_2)_3NH_2$ demonstraram um L_P de 89.40 $mL.h^{-1}.m^{-2}.mmHg^{-1}$ e um *cut-off* de 24.5 kDa, tendo-se verificado um aumento de L_P em 1.8 vezes, quando comparada com uma membrana pura de acetato de celulose. Observou-se, ainda, a total permeação da membrana às toxinas em estudo, ureia, creatinina e ácido úrico, e completa retenção da albumina. Adicionalmente, não houve evidências de colmatação da membrana durante o ensaio de filtração de longa-duração da albumina.

Palavras-chave: membrana híbrida monofásica; sol-gel; inversão de fases; purificação de sangue; ultrafiltração; filtração tangencial; convecção; hemodiálise

Contents

Preface i

Acknowledgments iii

Abstract v

Resumo vii

List of Figures xi

List of Tables xiii

Abbreviation List xv

1. Introduction 1

1.1. Fundamentals of membranes 2
  1.1.1. Membrane geometries and modules 5
  1.1.2. Phase inversion membranes 6
  1.1.3. Sol-gel technique 7
1.2. Pressure-driven processes. 8
1.3. Mass transfer in ultrafiltration processes 10
  1.3.1. Solvent and solute transport 10
  1.3.2. Polarization phenomena and fouling 11
  1.3.3. Boundary layer film model 13

2. Ultrafiltration membranes for blood purification 15

2.1. Hemodialysis and renal replacement therapies 15
2.2. Membranes for the artificial kidney 17
  2.2.1. Uremic syndrome and challenges of toxin removal 18
2.3. Motivation and thesis objectives 22

3. Materials and Experimental Methods 23

3.1. Materials 23
3.2. Membrane synthesis 24
3.3. Membrane drying process 27
3.4. Membrane characterization 28
  3.4.1. Scanning electron microscopy (SEM) 28
  3.4.2. Attenuated total reflection-Fourier transform infrared (ATR-FTIR) spectroscopy 28
3.5. Experimental setup 28
  3.5.1. Single hemodialysis membrane module (SHDMM) 28

3.5.2. Feed circulation circuit 31
3.5.3. Characterization of the SHDMM: pressure profile, pressure drop, transmembrane pressure, microchannel height, shear rate and shear stress at the wall 32
3.6. Permeation experiments under dynamic conditions 34
3.6.1. Water permeability 34
3.6.2. Molecular weight cut-off (MWCO) 35
3.6.3. Rejection coefficients to low-molecular weight water soluble uremic toxins 36
3.6.4. Bovine serum albumin filtration 37
4. Results and Discussion 39
4.1. Membrane characterization 39
4.1.1. Scanning electron microscopy (SEM) 39
4.1.2. Attenuated total reflection-Fourier transform infrared spectroscopy (ATR-FTIR) 41
4.2. Characterization of the SHDMM: pressure profile, pressure drop, transmembrane pressure, microchannel height, shear rate and shear stress at the wall 43
4.3. Permeation experiments under dynamic conditions 45
4.3.1. Water permeability 45
4.3.2. Molecular weight cut-off (MWCO) 47
4.3.3. Rejection coefficients to low-molecular weight water-soluble uremic toxins 48
4.3.4. Bovine serum albumin (BSA) filtration 51
Conclusions 53
Perspectives of future work 53
References 55
Appendix A. Pump calibration 61
Appendix B. TOC calibration curves 62
Appendix C. Uremic toxins calibration curves 63
Appendix D. BSA calibration curves 63

List of Figures

Figure 1-1. Simplified scheme of cross-flow filtration. Adapted from [19]. 2

Figure 1-2. Classification of synthetic and cellulosic membranes based on materials of construction, structural attributes, and configuration. Adapted from [20]. 3

Figure 1-3. Schematic cross-section representations of asymmetric membranes (integrally skinned and composite). Adapted from [24]. 4

Figure 1-4. Schematic representation of the filtration behavior of a) asymmetric and b) symmetric membranes. Adapted from [2]. 5

Figure 1-5. Ternary phase diagram representing the phase inversion process for polymer/solvent/non-solvent systems. Adapted from [15]. 7

Figure 1-6. Flux as a function of the applied transmembrane pressure for pure water and for an aqueous solution. 11

Figure 1-7. Boundary layer model for cross-flow filtration in which a concentration gradient is adjacent to the membrane surface. Adapted from [43]. 13

Figure 2-1. Representation of the extracorporeal blood circuit characteristic of hemodialysis. Adapted from [52]. 16

Figure 2-2. Schematic representation of a hollow fiber dialyzer and direction of blood and dialysate streams. Adapted from [24]. 17

Figure 2-3. Representation of human serum albumin. Domains I, II and III are shown in purple, blue and green, respectively; each of them comprising two subdomains A and B. Also represented are α-helices, as cylinders, and ligand binding site Sudlow's site I in subdomain IIA and Sudlow's site II in subdomain IIIA. Adapted from [76]. 21

Figure 3-1. Cellulose-acetate structure (**A**) and sol-gel silica precursors: TEOS (**B**) and APTES (**B**). 24

Figure 3-2. Schematic representation of the single hemodialysis membrane module (SHDMM). Unit I seals the feed flow chamber, represented by unit II. Unit V seals the permeate collecting chamber, represented by unit IV. Unit III is the supporting surface for the membrane to be tested. 29

Figure 3-3. Fluid flow in a narrow plane slit. Adapted from [88]. 30

Figure 3-4. Schematic representation of the experimental setup used for permeation experiments under dynamic conditions. 32

Figure 3-5. Pressure profile of the circuit during the circulation of DI water through the SHDMM circuit at different values of Q_F, which are delimited by the dashed lines. The pressure data is colour-coded according to the different sensors: black line P1, red line P2, green line P3, and dark blue line P4. ... 33

Figure 4-1. SEM images of the CA-SiO_2-$(CH_2)_3NH_2$ (**A**, **C** and **E**) and CA (**B**, **D** and **F**) membranes. **A**, **B**: top active layer (×1000). **C**, **D**: cross-section (×700) where the red lines indicate the membranes' thickness. **E**, **F**: bottom porous surface (×4000). 40

Figure 4-2. Wide-range ATR-FTIR spectra (4000-650 cm^{-1}) of the CA-SiO_2-$(CH_2)_3NH_2$ and CA membranes. 41

Figure 4-3. ΔP (red line) and TMP (black line) values obtained for the flow of DI water through the SHDMM circuit at different values of Q_F, which are delimited by the dashed lines. 43

Figure 4-4. Ultrafiltration flux of pure water at 37°C as a function of the transmembrane pressure for the hybrid CA-SiO_2-$(CH_2)_3NH_2$ membrane, according to the three hypotheses. The membrane permeation area in the O-ring, Laminar and Cell-Perforated cases, was 105, 60 and 20.9 cm^2. 45

Figure 4-5. Ultrafiltration flux of pure water at 37°C as a function of the transmembrane pressure for CA-SiO_2-$(CH_2)_3NH_2$ (■) and pure CA (○) membranes. The dotted lines represent the linear fit which enables the determination of each membrane L_P. 46

Figure 4-6. Rejection coefficient profiles of the CA-SiO_2-$(CH_2)_3NH_2$ (**A**) and CA (**B**) membranes to solutes with increasing molecular weights: 400, 3000, 6000, 10000, 20000 and 35000 Da. The horizontal full lines are set for a rejection of 90%, i.e. $\log R1\text{-}R=0.95$. The dashed rejection lines represent the linearization of the rejection coefficients obtained for 3 different molecular weight solutes: 10000, 20000 and 35000 Da. The dotted dropdown lines indicate the estimated MWCO according to the method employed. 48

Figure 4-7. Concentration profiles of urea, creatinine, and uric acid for CA-SiO_2-$(CH_2)_3NH_2$ (**A**, **C** and **E**) and CA (**B**, **D** and **F**) membranes, regarding feed (■) and permeate (○) samples, for a total experiment time of 105 minutes. The initial feed concentrations aim to represent those of uremic populations. 49

Figure 4-8. BSA concentration profiles for CA-SiO_2-$(CH_2)_3NH_2$ (A) and CA (B) membranes, regarding feed (■) and permeate (○) samples, for a total experiment time of 465 minutes. 51

List of Tables

Table 1-1. Technically relevant pressure-driven membrane separation processes, their operating principles, and their application. Adapted from [2,39]. 9

Table 2-1. Different classes of uremic toxins, as proposed by the EUTox [70]. 19

Table 3-1. Casting solution compositions, on weight basis. 25

Table 3-2. Hybrid membrane composition, on molar basis. 27

Table 4-1. Assignment of the ATR-FTIR spectra bands of the active layer of the hybrid and pure CA membranes. 42

Table 4-2. Pressure drop registered throughout the hydraulic permeability experiment, corrected values taking into account the distance between the sensors and the SHDMM, and microchannel height in each scenario. 44

Table 4-3. Hydraulic permeability values obtained for the hybrid CA-SiO_2-$(CH_2)_3NH_2$ and pure CA membranes, at 37ºC and 25ºC. 47

Abbreviation List

2B	Channel height
A	Area
AK	Artificial kidney
APTES	3-(triethoxysilyl)-propylamine
ATR-FTIR	Attenuated total reflection-Fourier transform infrared
AVF	Arteriovenous fistula
B	Channel half-height
BSA	Bovine serum albumin
CA	Cellulose acetate
C_B	Concentration of the bulk solution
CKD	Chronic kidney disease
C_W	Concentration at the membrane surface
DI	Deionized water
ESRD	End stage renal disease
EUTox	European Uremic Toxin Group
GFR	Glomerular filtrate rate
GS	Gas separation
HD	Hemodialysis
HDF	Hemodiafiltration
HF	Hemofiltration
HSA	Human serum albumin
J	Ultrafiltration flux
J_∞	Limiting flux
J_m	Mass flux
K_{UF}	Ultrafiltration coefficient
L	Length
L_P	Hydraulic permeability
MF	Microfiltration
MW	Molecular weight
MWCO	Molecular weight cut-off
NDIR	Non-dispersive infrared
NF	Nanofiltration
PAN	Polyacrylonitrile
PBS	Phosphate buffer saline
PBUT	Protein-bound uremic toxin
PD	Peritoneal dialysis
PEG	Polyethylene glycol
PS	Polysulfone

Q_F	Feed flowrate
R	Rejection coefficient
RO	Reverse osmosis
SEM	Scanning electron microscopy
SHDMM	Single hemodialysis membrane module
t	Time
T	Temperature
TEOS	Tetraethyl orthosilicate
TMP	Transmembrane pressure
TOC	Total organic carbon
UF	Ultrafiltration
UT	Uremic toxin
V	Volume
v_z	Velocity in the z-direction
$v_{z,\ avg}$	Average velocity in the z-direction
$v_{z,\ max}$	Maximum velocity in the z-direction
W	Width
δ	Thickness
ΔP	Pressure drop
λ_{max}	Wavelength of maximum absorbance
μ	Viscosity
ρ	Density
τ	Shear stress
Υ	Shear rate
$\vec{v}$	Velocity vector
$\dot{m}$	Mass flowrate

1. Introduction

Life as we know it, knows not how to thrive without membranes. Indeed, they are one of the main constituents of every living cell but more surprisingly, they have scaled-up into our daily lives. Since 1965, membrane technology has earned its prominent role in industrial applications, displacing conventional separation processes – a deed mainly owing to the capital and energy efficiency of membrane processes [1]. Their applications range from desalination of seawater and brackish water, assuring water supply to areas with no access to alternative sources, to integrated steps for cheese and wine production. They are the core components of fuel cells and electrolysis, besides playing an active role in the efficiency of hydrogen production and processing in refineries, and enabling the concentration and purification of macromolecular solutions in the food and drug industry [2]. But perhaps more remarkably, membranes have been incorporated in medical and engineering processes, such as the field of artificial organs.

Artificial organs comprise complex medical devices with active mechanical or biomechanical functions that aim on duplicating or augmenting a specific function in the human body [3,4]. They can be either surgically implanted or extra corporeal – in which the blood is temporarily processed outside the patient’s body. Among these devices are those that mimic functions of the heart, lungs, kidneys, liver and pancreas [4].

Recently, KidneyX, a public-private partnership between the U.S. Department of Health and Human Services and the American Society of Nephrology launched the Artificial Kidney Prize, a competition that intends on accelerating artificial kidney development toward human clinical trials [5]. The motivations underlying this endeavor derive from chronic kidney disease (CKD), a growing public health concern affecting 11-13% of the global population [6], defined by an irreversible worsening of renal function which can lead to end stage renal disease (ESRD). The progressive loss of kidney function is linked to the retention of metabolic waste products, also known as retention solutes or uremic toxins (UTs), normally excreted by healthy kidneys. Currently, about 3 million ESRD patients receive renal replacement therapies to survive, either in the form of dialysis or, in the case of a small subgroup, kidney transplantation [7].

Kidney transplantation is, on average, associated with better clinical outcomes than dialysis. However, kidney transplant rates are lessened by the scarcity of donors, infection risks and sequelae of life-long immunosuppression [8].

Hemodialysis (HD) is used to re-establish body water solute concentrations that cannot be achieved by the natural organ and comprises the vast majority of kidney replacement therapy worldwide [8–10]. The hemodialyzer is the key component of the extracorporeal blood circulation circuit as it is responsible for removing accumulated uremic toxins and water while simultaneously retaining vital blood components, such as proteins, through a bundle of semi-permeable membranes [11]. In this sense, the dialyzer acts as an artificial kidney.

The following sections will display an overview on membrane fundamentals and membrane processes, culminating on membrane advances towards blood purification devices.

1.1. Fundamentals of membranes

A membrane is defined as a permselective barrier, or interphase, that establishes a boundary between two phases and allows preferential permeation of certain species, while retaining others [2,12]. The membrane controls the exchange of mass between two bulk phases, impelled by a driving force. The latter may be caused by diffusion of individual molecules or by convection induced by gradients in electrical potential, concentration, pressure or temperature [13,14].

In membrane processes, two types of filtrations can be distinguished, namely, dead-end and cross-flow filtration, with the latter being represented in Figure 1-1. These can be distinguished with regard to the direction of the feed stream relative to the orientation of the membrane surface.

Dead-end filtration is the most common process for small-scale separation, especially in water treatment. In this approach, the feed and permeate are both perpendicular to the surface of the membrane. This filtration is, however, prone to fouling, consequently leading to increased resistance and reduced permeate flux [15–17].

Cross-flow filtration refers to the system in which the feed flows parallel, or tangentially, to the membrane surface. The shear force exerted by the flowing feed stream on the membrane surface aids the removal of deposits that cause a decrease of permeate flux [18]. Hence, this mode is particularly useful for filtering highly concentrated solutions, macromolecules, or even larger components such as cells and proteins [15,16]. When compared to dead-end filtration, more complex equipment is required, resulting in increased operating costs due to the higher energy requirements to circulate the feed flow [18].

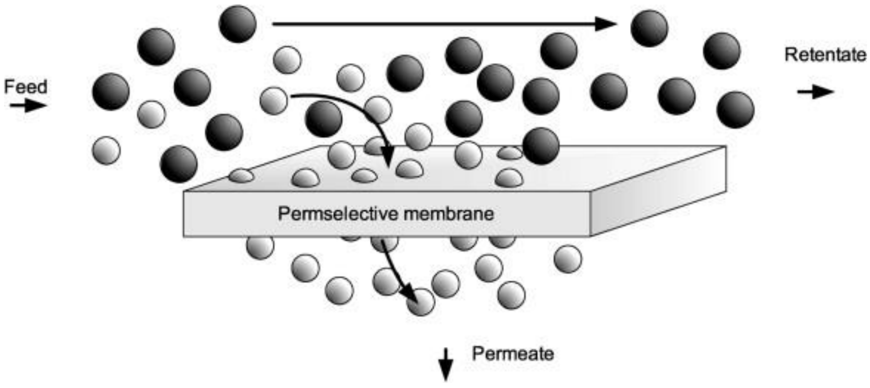

Figure 1-1. Simplified scheme of cross-flow filtration. Adapted from [19].

The feed stream is constituted by an aqueous solution of a certain solute, or a mixture of solutes, and flows tangentially to the permselective membrane. Filtration occurs perpendicular to the membrane and the permeate stream is composed by the preferentially permeated solutes and water. The retentate stream, on the other hand, is enriched with the least permeable components, that is, the solutes that have been rejected by the membrane [1,15]. Furthermore, selectivity and thus, performance, of a membrane to a fluid mixture is generally expressed by the rejection coefficient (R), a parameter reflecting the fraction of solute that is actively rejected by the membrane [2,12,15].

The composition and structure of a membrane dictate not only its performance but most importantly its function [14]. To a certain extent, membranes can be tailormade so that their separation properties meet the requirements of a specific separation task.

Figure 1-2 schematically shows the classification of according to their morphology, contemplating symmetric and asymmetric cross-section structures.

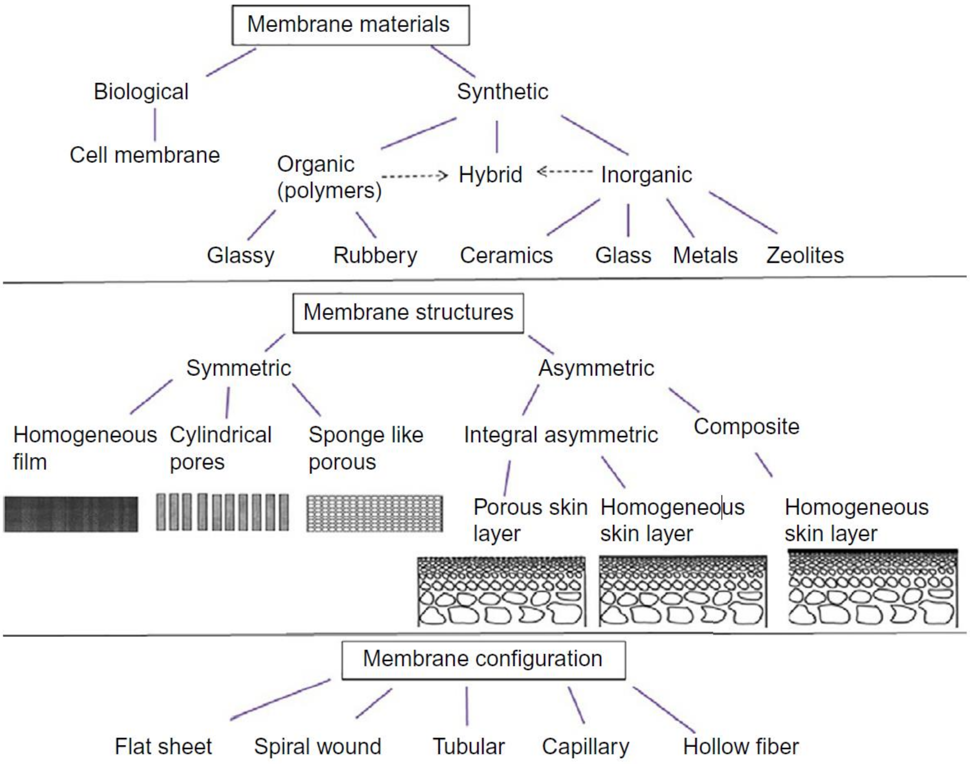
Membrane materials
Biological
Synthetic
Cell membrane
Organic (polymers)
Hybrid
Inorganic
Glassy
Rubbery
Ceramics
Glass
Metals
Zeolites
Membrane structures
Symmetric
Asymmetric
Homogeneous film
Cylindrical pores
Sponge like porous
Integral asymmetric
Composite
Porous skin layer
Homogeneous skin layer
Homogeneous skin layer
Membrane configuration
Flat sheet
Spiral wound
Tubular
Capillary
Hollow fiber

Figure 1-2. Classification of synthetic and cellulosic membranes based on materials of construction, structural attributes, and configuration. Adapted from [20].

Symmetric membranes are characterized by having uniform cross-section structures, which may be porous or non-porous, in the case of symmetric microporous and symmetric dense membranes, respectively. The latter consists on a dense homogeneous film where separation of different chemical species takes place according to their solubility in the film [2,14]. The resistance to mass transfer in symmetric membranes is determined by the total membrane thickness, which ranges roughly from 10 to 200 μm [12]. These membranes are widely used in processes such as dialysis, microfiltration and ultrafiltration [20].

Asymmetric membranes are characterized by a non-uniform cross-section structure, comprising a very thin (0.1 to 1 μm) active top dense layer (or skin layer) on a highly porous, thicker (50 to 200 μm) sublayer [2,20,21]. The top dense layer governs the selectivity and performance of the membrane and is largely responsible for the resistance to mass transfer [12], while the porous sublayer provides mechanical strength to the membrane and has a negligible effect on the selectivity properties [2,22]. The nature of the dense skin layer (type of polymer, available spaces between polymer chains and/or pore size, etc.) is responsible for selectivity characteristics and the membrane thickness is intimately related to the mass transport properties. Specifically, the mass transport rate is inversely proportional to the resistance of the membrane, which in turn is inversely proportional to the mass transport coefficient [2]. Asymmetric membranes are primarily used in pressure-driven separation processes, including reverse osmosis, nanofiltration, ultrafiltration, microfiltration and gas separation [20,23].

Figure 1-3 shows the schematic representation of asymmetric membranes. When the material of the top dense layer and the porous sublayer of an asymmetric membrane are the same, the membrane is referred to as an integrally skinned asymmetric membrane. These types of membranes are typically prepared through the phase inversion technique which is discussed in section 1.1.2. On the other hand, if the material of the top skin layer is different from the material of the porous sublayer the membrane is designated by a composite membrane, which is generally obtained by depositing an extremely thin polymer film on a microporous substructure [2,22,23].

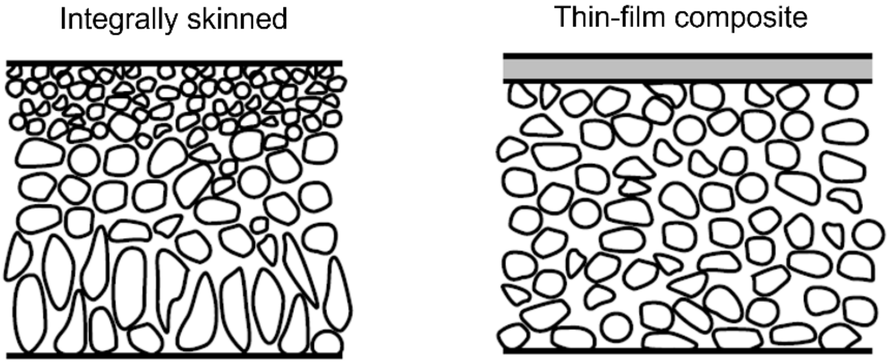

Figure 1-3. Schematic cross-section representations of asymmetric membranes (integrally skinned and composite). Adapted from [24].

In contrast to the microporous symmetric membranes, which act as traditional filters that often retain particles in their pores with subsequent fouling and decline of permeation fluxes, the asymmetric membranes act as surface filters retaining the rejected material at the membrane surface, before the solutes reach the pores of the porous substructure, and therefore avoiding or delaying pore blocking and fouling [21], as depicted in Figure 1-4. Furthermore, the rejected material is prone to be removed by shear forces at the membrane surface imposed by the parallel flow of the feed stream [2].

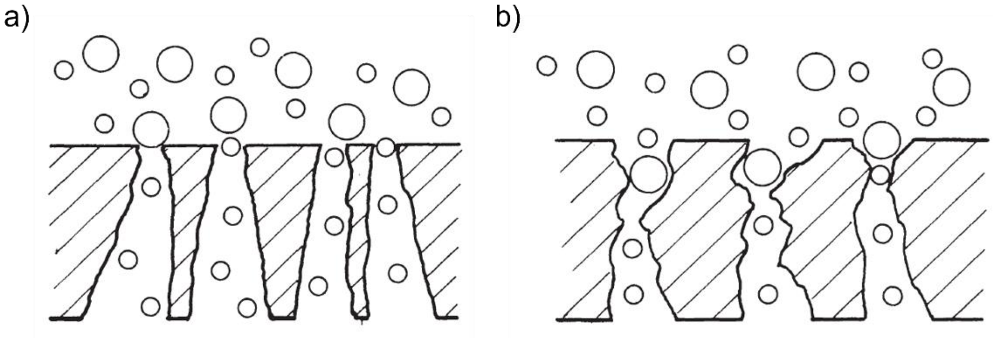

Figure 1-4. Schematic representation of the filtration behavior of a) asymmetric and b) symmetric membranes. Adapted from [2].

Asymmetric membranes have a central place in membrane separation technology due to the fact that they combine the high selectivity of a dense membrane with high permeation fluxes of thin membranes [2,21]. These membranes are primarily used in pressure-driven processes, such as reverse osmosis and ultrafiltration, which are discussed in section 1.2.

1.1.1. Membrane geometries and modules

In an industrial scenario, where hundreds to thousands of square meters of membranes are required to perform the required separation process, the economic and efficient packaging of large membrane areas is of imperative need [24]. There are four types of membrane modules used in applications, namely, plate-and-frame, tubular, spiral-wound and hollow fiber [15,18].

The plate-and-frame is the earliest and simplest configuration but apart from being cost-intensive, is associated with leaks caused by the gasket seals [18,24]. They are employed in pervaporation systems and in a limited number of highly fouling reverse osmosis and ultrafiltration applications. Tubular modules are contemporary to the plate-and-frame but are now generally limited to ultrafiltration applications, for which the benefit of resistance to membrane fouling outweighs their high cost [24].

Currently, due to their relatively high cost, tubular and plate-and-frame modules have been displaced by two other designs: the spiral-wound and the hollow fiber modules.

Spiral-wound modules were originally used in a number of early artificial kidney (AK) designs but were fully developed for reverse osmosis systems. These have a similar configuration to the plate-and-frame system but with the advantage of a larger filtration area per unit volume of the module [15]. Hollow-fiber modules are especially attractive, since their simple design allows large membrane areas to be contained in an economical system. They are used in gas separation, hemodialysis, and ultrafiltration.

Although the module choice is greatly influenced by economic considerations, its functionality is determined by the type of application and should take into account factors such as packing density, fouling tendency and cleaning procedures [12].

1.1.2. Phase inversion membranes

Phase inversion is a versatile technique that allows various filtration characteristics and morphologies to be obtained, whereby a polymer is transformed in a controlled manner from a liquid state into a swollen three-dimensional macromolecular complex [12,14]. There are a number of phase inversion routes occurring in the fabrication of polymeric membranes, including immersion precipitation, thermally-induced phase separation, evaporation-induced phase separation and vapor-induced phase separation [15].

Integrally skinned asymmetric membranes are most commonly obtained through immersion precipitation or wet-phase inversion. In this technique, the polymer is dissolved in a suitable solvent or solvent mixture. The resulting polymer solution is cast into a film with thickness in the order of 100-500 µm [20,23] on a suitable, inert support, by means of a casting knife. The cast film is then immersed in a nonsolvent or coagulation bath – water is usually preferred from an environmental point of view, but organic solvents can be used as well. After immersion, the solvent will diffuse into the coagulation bath, whereas the nonsolvent will diffuse into the cast membrane film. During this process, the polymer solution will eventually become thermodynamically unstable, allowing the formation of a two-phase system during liquid-liquid demixing: a polymer-rich phase, which upon solidification will ultimately constitute the structure of the membrane, and a solvent-rich phase, forming the liquid-filled membrane pores [12,15,25].

Figure 1-5 shows a ternary phase diagram which is generally used to explain the precipitation pathway of the casting solution during polymeric membrane formation by phase inversion.

The path from A to D, indicated by the dashed line, represents the phase inversion route of a polymeric solution. In a first step, the original polymeric solution (point A in the binary diagram solvent-polymer) is immersed into a non-solvent bath, whereby the exchange of solvent from the polymeric solution with the non-solvent from the bath occurs. This phenomenon comprehends two regions: the monophasic domain (dashed line between A and B) and the biphasic domain (dashed line between B and D).

In the monophasic domain, during the solvent/non-solvent exchange, the polymer concentration at the surface increases, causing a decrease in the exchange speed of the process. Upon reaching the miscibility gap (point B) and entering the biphasic domain, the polymer reaches its solubility limit and starts to precipitate. Here, the continuous replacement of the solvent by the non-solvent will induce solidification of the polymer-rich phase (point C), after which the asymmetric structure of the membrane will be achieved. Eventually, the solution reaches point D, where both solid and liquid phases are in equilibrium (S-L tie-line). A solid, polymer-rich phase which forms the membrane structure is represented by point S and a liquid phase, which constitutes the membranes pores filled with non-solvent is represent by point L [25,26].

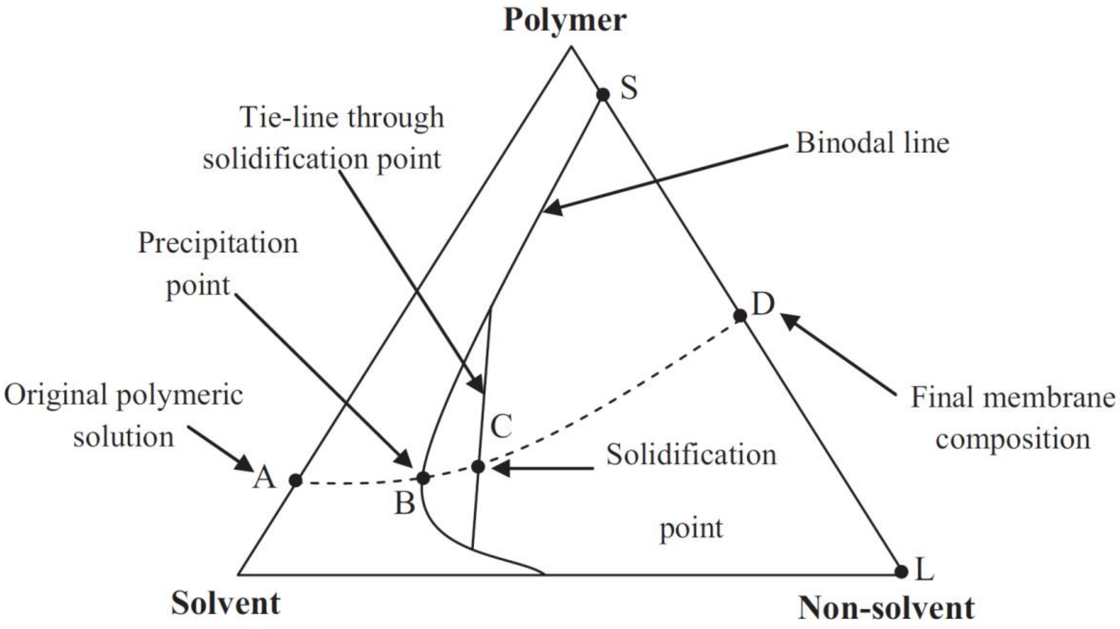
Polymer
S
Tie-line through solidification point
Binodal line
Precipitation point
D
Original polymeric solution
Final membrane composition
C
A
B
Solidification point
L
Solvent
Non-solvent

Figure 1-5. Ternary phase diagram representing the phase inversion process for polymer/solvent/non-solvent systems. Adapted from [15].

The performance characteristics of phase inversion membranes depend on two factors: i) casting solution composition (polymer:solvent ratio, type of solvent or solvent system, temperature, etc.) and ii) casting conditions (solvent evaporation time, humidity, temperature, coagulation medium, etc.) [14].

Furthermore, asymmetry in membrane structure results of the more rapid desolvation which occurs at the interface between the polymer solution and the gelation medium [27].

1.1.3. Sol-gel technique

The sol-gel process is a bottom-up approach that represents a powerful and versatile strategy for the preparation of functional inorganic and hybrid materials that facilitate control over the molecular composition, as well as organization of the materials at the various length scales [28]. The term sol-gel is associated with the chemical transformation of a system from a colloidal suspension of submicrometer-sized particles in a monomer solution, or a liquid sol, into a three-dimensional interconnecting network phase, or a gel [28–30]. The transition between the sol into the gel phase is achieved via controlled hydrolysis and condensation of inorganic (e.g., halide or nitrate metal salts) or metal-organic (e.g., metal alkoxides) precursors within a solvent, upon the addition of a catalyst (e.g., a base or an acid). The resulting material consists of a continuous solid backbone with high porosity that encloses the liquid phase [28]. Applications of functional materials derived from sol-gel include fields such as controlled release, protective coatings, adsorption and separation [31].

Moreover, the sol-gel reaction conditions are mild, in the sense that they mostly take place at room temperature and pressure, and the ability to synthesize solid-sate materials from molecular precursors not only provides control over the composition, purity and homogeneity of the materials, but also enables the molecular organization to be precisely manipulated [28,32]. Aside from the composition and microstructure control at the molecular level, sol-gel provides the ability to shape the material by casting bulk gels in precision molds, spinning fiber or dip coating thin films [33]. The result is an increased chemical, mechanical and thermal stability without compromising the properties of the polymers [34,35].

The sol-gel synthesis of silica is based on the hydrolysis and condensation of silicon alkoxides. Hydrolysis generates reactive silanol groups, whereas condensation leads to the formation of bridging oxygen. Since its inception, sol-gel methods have typically involved the use of tetraethyl orthosilicate (TEOS) as a principal silica forming agent. The first reason for using TEOS is the ease of sol-gel hydrolysis and condensational reactional processes, followed by the formation of robust networks with tunable reactivity and a high degree of control, affordable through simple variations in the synthesis conditions, such as pH, temperature, and additives. Other reasons include the ease of in situ functionalization through the incorporation of organic molecules, polymers, and biomolecules in the reaction vessel [36].

As silicon alkoxides are not very sensitive to hydrolysis, the addition of an acid or base catalyst promotes enhanced hydrolysis and condensation rates [37]. At the function group level, three bimolecular nucleophilic reactions are generally used to describe the sol-gel process, through hydrolysis and subsequent condensation of silicon alkoxides [33]:

$$\equiv\text{Si-OR} + \text{H}_2\text{O} \rightleftharpoons \equiv\text{Si-OH} + \text{ROH} \tag{1-1}$$

$$\equiv\text{Si-OR} + \text{RO-Si}\equiv \rightleftharpoons \equiv\text{Si-O-Si}\equiv + \text{ROH} \tag{1-2}$$

$$\equiv\text{Si-OR} + \text{HO-Si}\equiv \rightleftharpoons \equiv\text{Si-O-Si}\equiv + \text{H}_2\text{O} \tag{1-3}$$

The hydrolysis reaction (Equation 1-1) replaces alkoxide groups with hydroxyl groups. Subsequent condensation reactions involving the silanol groups produce siloxane bonds and the by-products alcohol (Equation 1-2) or water (Equation 1-3).

1.2. Pressure-driven processes.

Membrane processes are continuous steady-state operations, which are mostly pressure-driven and rely on the use of synthetic or cellulosic membranes [1,13,38]. Among pressure-driven membrane processes are microfiltration (MF), ultrafiltration (UF), nanofiltration (NF), reverse osmosis (RO) and gas separation (GS). The classification spectrum for these processes relies on the pore size of the membranes and applied pressure [20], as described in Table 1-1.

Table 1-1. Technically relevant pressure-driven membrane separation processes, their operating principles, and their application. Adapted from [2,39].

Separation process	Membrane type	Driving force	Method of separation	Range of application
Microfiltration (MF)	Symmetric microporous membrane 0.1 to 10 µm pore radius	Hydrostatic pressure difference 0.1 to 1 bar	Sieving mechanism due to pore radius and absorption	Sterile filtration clarification
Ultrafiltration (UF)	Asymmetric microporous membrane 1 to 10 nm pore radius	Hydrostatic pressure difference 0.5 to 5 bar	Sieving mechanism	Separation of macromolecular solutions
Nanofiltration (NF)	Thin film composite membrane 0.5 to 2 nm	Hydrostatic pressure difference 5 to 40 bar	Sieving Solution-diffusion mechanism	Separation of salt and microsolutes from solutions
Reverse osmosis (RO)	Integrally skinned asymmetric membrane	Hydrostatic pressure 20 to 100 bar	Solution-diffusion mechanism	Separation of salt and microsolutes from solutions
Gas separation (GS)	Homogeneous or porous polymer	Hydrostatic pressure concentration gradient	Solubility, diffusion	Separation from gas mixture

MF is the oldest membrane process using dead-end filtration, with the advantages of very low capital cost and the recovery of a highly concentrated feed. Its separation mechanism is not only based on sieving, where the particles whose sizes are smaller than the pore size of the membrane are permeated while the larger particles are rejected; instead, in many cases, the particles to be separated are in fact adsorbed onto the surface of the pore, resulting in a significant reduction in pore size, contributing to fouling effects [1]. MF is primarily used in liquid clarification, removal of microorganisms from fermentation products during downstream processing and wastewater treatment.

UF processes make use of membranes with asymmetric structures, where a dense skin layer is determinant on the resistance to mass transfer. Similarly to MF, UF processes operate at low pressures, typically between 0.5 to 5 bar [2,39], where the pressure gradient governs mass transport through the convective flux within the membrane. In such processes, a solution containing a solute of molecular size notably greater than that of the solvent molecule is removed by the application of a hydraulic pressure. Hence, the selectivity of UF membranes is based on the difference in solute size, membrane properties and hydrodynamic conditions [15,40]. UF membranes are often operated in a tangential flow mode, thereby maximizing flux rates and filter life [2,21]. UF is perhaps the most widely used membrane process, next to MF, and intend on performing feed clarification, concentration of rejected solutes and fractionation of solutes, as well as treatment of industrial wastewater [13]. Interestingly, the convective properties of UF have been notably applied to renal replacement therapies such as hemodialysis [2]. UF is addressed in greater detail in section 1.3.

NF membranes are used in processes wherein particles and dissolved macromolecules smaller than 2 nm are rejected, thus being suited for rejection of low molecular weight organic compounds and multivalent ions, with its largest application being in water softening [21,41]. In RO membranes, the applied transmembrane pressure instigates selective movement of a solvent against its osmotic pressure difference [20]. This process removes most of the dissolved contaminants in water, thereby being widely used in potable water treatment plants [15]. In pair with NF, RO processes have high pressure requirements, which translates in high capital investments.

As we move from MF through UF to NF, the size or molecular weight of the molecules to be separated diminishes and consequently the pore sizes in the membrane must become smaller. This implies that the resistance of the membranes to mass transfer increases and hence the applied pressure acting has the driving force has to be increased. [12]

GS mostly resorts to nonporous symmetric membranes and is generally applied for hydrogen and natural gas separation, as well as CO_2 capture. Compared to conventional technology used in GS, membrane technology offers minimal operating cost. The mechanisms by which the mechanism acts are strongly dependent on pore size distribution of the membrane, operating temperature and pressure, and nature of the membrane and permeating molecules [15].

1.3. Mass transfer in ultrafiltration processes

1.3.1. Solvent and solute transport

The pure water flux through a membrane is directly proportional to the applied pressure, and can be plotted as a straight line, according to Figure 1-6, which is representative of an ultrafiltration scenario. However, when an aqueous solution is considered and the transmembrane pressure increases, the flux follows a similar trend to that of pure water until it reaches the maximum flux, or limiting flux, J_∞. This constant is dependent on the nature of the feed and operating conditions, such as shear rate at the membrane, on the concentration in the bulk feed and on the mass transfer coefficient [12].

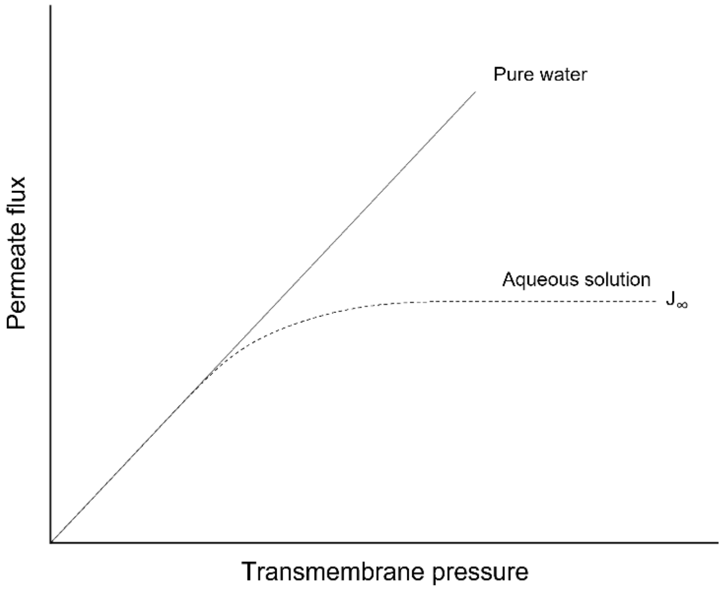

Figure 1-6. Flux as a function of the applied transmembrane pressure for pure water and for an aqueous solution.

Flux decline, as depicted in Figure 1-6 is linked to the resistance inherent to a membrane separation process. Aside from the evident resistance posed by the membrane itself, several other factors can contribute to an impaired mass transfer, among them concentration polarization.

In UF and MF processes, the separation mechanism is broadly considered to be one of sieving where an increase in the applied pressure increases the flux. However, the effect of concentration polarization limits the practical flux rates due to a build-up of solute on the feed side of the membrane in the concentration boundary layer. At sufficiently high pressures, gelation of the macromolecules can occur resulting in the formation of a thin gel layer on the surface which can also act as a secondary membrane [14].

1.3.2. Polarization phenomena and fouling

Fouling is a major concern, especially in pressure-driven membrane separation processes, and is defined as the deposition of retained particles on the membrane surface or inside its structure and occurs mainly in MF and UF, where porous membranes which are implicitly susceptible to fouling are used [12]. Conventional cleaning such as backwashing can remove the fouling, but with low efficiency. In this regard, alternative treatments have been suggested. Physical treatment has the ability to remove loose particles attached to the surface of the membrane, whereas chemical cleaning is used to remove adhered particles.

The reduction of membrane performance, translated in the decline of permeate flux, shortening of the membrane life span and incurring high cost due to the high transmembrane pressure requirements, results not only from the fouling events but also from the concentration polarization, pore blocking, adsorption and gel layer formation [12,18]. These factors induce additional resistance on the feed side to the transport across the membrane.

Fouling and concentration polarization are commonly misconceived as one and the same; despite not being completely independent of each other, their distinction can rely on time-dependence: a continuous flux decline is attributed to fouling, while a decrease with subsequent flux stabilization over time reflects concentration polarization. Furthermore, a flux reduction that is reversible is usually associated to concentration polarization, whereas an irreversible flux reduction is due to fouling.

Concentration polarization is a reversible occurrence whereby a concentration gradient is created between the concentrations of nonpermeating species due to accumulation of retained molecules at the membrane surface, where a boundary layer is formed. Polarization phenomena are inherent to membrane separation processes and linked to high fluxes, and its effect is especially severe in ultrafiltration. Indeed, a combination of high fluxes and high solute retention translates into the formation of a gel layer on the surface of the membrane, representing the maximum concentration of a given solute. As the solute reaches its maximum concentration at the membrane surface and is not capable of any further increase, the gel layer becomes thicker, implying an increase in the resistance of the gel layer to mass transport [13]. In the limiting flux region (Figure 1-6) an increase in pressure leads to an increase in the resistance of the gel layer, resulting in a constant flux. The gel concentration depends on size, shape, chemical structure and degree of solvation but is independent of the bulk concentration [12].

In turn, pore blocking occurs when the particulates or solutes with small size distributions are introduced to the membrane body, and this can cause severe fouling.

Despite being a complex phenomenon related to feed solution properties, nature of the membrane and operating conditions, control of fouling and polarization can be achieved, for instance, by modifying the membrane surface and optimizing operating conditions [18]. Increasing the feed velocity parallel to the membrane and, consequently the shear rate at the membrane surface, adequate cleaning methods, and changing the module shape and dimensions, for instance by decreasing the module length, are solutions to be considered. As aforementioned, porous membranes are more susceptible to fouling, such that a narrow pore size distribution can reduce fouling [14]. Furthermore, the use of hydrophilic rather than hydrophobic membranes should be preferred, since proteins adsorb more strongly at hydrophobic surfaces and are less readily removed than at hydrophilic surfaces [42].

The resistance to permeation of a membrane is a function of the membrane pore size, feed stream components, and the degree to which gel layer formation and fouling layer formation occur. Increasing the feed stream circulation rate will, as a general rule, reduce gel layer thickness and increase flux. Operation within the turbulent flow regime, may significantly enhance permeation by reducing both gel layer and fouling layer thickness through improved transfer of solids from the membrane surface back into the bulk stream [14].

1.3.3. Boundary layer film model

A simplistic approach to the concentration polarization consists of assuming the existence of a thin layer of fluid, with thickness δ, between the membrane surface and the bulk solution, wherein concentration gradients govern mass transfer [24].

The fluid flow in a channel typically exhibits a higher velocity in the center rather than near the surface, an effect that is mainly due to shear stress effects and fluid viscosity. At the surface of the membrane, the fluid velocity is zero and close to it, there is a small region of variable velocity – boundary layer [14].

The boundary layer can be considered as a concentrated solution through which solvent molecules permeate, with the permeability of this stagnant layer depending very much on the concentration and the molecular weight of the solute. The resistance exerted by this layer is far much greater for macromolecular solutes than for low molecular weight solutes [12].

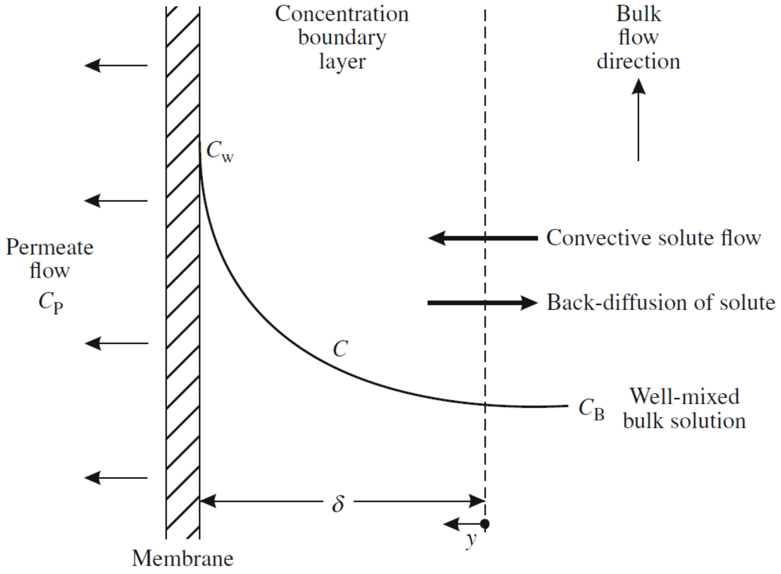

Figure 1-7. Boundary layer model for cross-flow filtration in which a concentration gradient is adjacent to the membrane surface. Adapted from [43].

The extent of concentration polarization is determined by the increase or decrease of the permeate concentration at the membrane surface, C_W, compared to the bulk solution concentration, C_B. A measure of the extent of this phenomenon can be calculated through the ratio of these two concentrations – the concentration polarization modulus [12,24]. When the modulus assumes the value of 1.0, no concentration polarization occurs, but as the modulus deviates farther from 1.0, the effect of polarization on membrane selectivity and flux becomes increasingly important.

The most straightforward method of minimizing concentration polarization is to reduce the boundary layer and it could be done by increasing the feed flow velocity and thus, inducing turbulence mixing at the membrane surface [24,38].

2. Ultrafiltration membranes for blood purification

Blood purification therapies are based on the extracorporeal treatment of blood and are widely used for the treatment of many disorders that are refractory to conventional therapies – like drug administration or surgery [44]. Its mechanism of action is based on the removal of toxins or pathogenic agents from blood circulation through techniques including filtration, adsorption, or a combination of both. Due to its capacity in direct and rapid removal of pathogenic agents from patients, blood-purification therapy is employed in life support for organ failure. In this context, it is mostly applied through hemodialysis, used in the treatment of patients with renal failure. Suffice to say that these therapies are life-preserving treatments instead of a cure.

2.1. Hemodialysis and renal replacement therapies

The kidney is of paramount importance on the body's waste disposal and acid-base regulation mechanisms, and its function can be characterized by a key parameter: the glomerular filtrate rate (GFR) [24,45]. The level of GFR correlates well, albeit not perfectly, with the likelihood of chronic kidney disease (CKD) associated to complications such as uremic syndrome, cardiovascular disease and anemia. A GFR below 60 mL/min/1.73 m^2 together with the presence of protein in the urine sufficient to establish the diagnosis of CKD [45,46]. GFR quantification generally consists on evaluating the serum creatinine concentration to estimate kidney function and takes into account parameters that correlate with muscle mass such as age, sex, and body size [45].

As the GFR of renal patients decreases, the severity of CKD increases and most times than not, leads to end stage renal disease (ESRD) wherein patient survival is dependent on dialysis or kidney transplantation. The shortage of organ donors and related complications prevents transplants from being available to the vast majority of ESRD patients, thus leaving dialysis as the best alternative. Among dialysis therapy, two main modalities can be distinguished. Peritoneal dialysis (PD) relies on the lining of the abdomen – peritoneum – to act as a membrane, allowing exchange of toxins and extra fluid from the blood onto the dialysate, which is injected in the patient's abdomen and drained out usually after 4-6 hours [47]. On the other hand, hemodialysis remains the leading modality by which ESRD care is delivered worldwide [48]. Each HD session performed in a dialysis center last for about 4 hours, at least three times per week [49,50]. Conventional HD is based on diffusive transport of solutes and is mainly effective on removing water-soluble small molecular weight solutes whereas the removal of solutes with larger molecular sizes is limited by diffusive resistance, such as β_2-microglobulin [48]. Thus, there has been significant effort since the 1970s to develop other dialysis modalities that mainly rely on convective mechanisms, namely hemofiltration (HF) and hemodiafiltration (HDF).

The ultimate innovation in these techniques is the fact that they combine diffusive and convective solute transport but, unlike conventional HD and HDF, HF exemptss the use of a dialysate solution. Some of the molecular species cleared by the human kidney are known to be of a higher molecular weight than those removed in artificial kidneys. It has been speculated that these 'middle molecules' are in some way responsible for the lack of complete well-being suffered by artificial kidney users. In hemodiafiltration, blood is ultrafiltered rather than dialyzed, and small as well as middle molecules are removed with the ultrafiltrate [2]. These three therapies share, nevertheless, a similar blood circuit.

Blood cleansing resorts to an extracorporeal blood circuit which comprises the blood and dialysate compartments, and the membrane interface, enclosed in a dialyzer or artificial kidney.

The first successful hemodialyzer was constructed by Kolff in 1945. Kolff's device used dialysis to remove urea and other waste products directly from blood. A flat cellophane sausage casing formed the dialysis membrane, which was wound around a rotating drum immersed in a bath of saline. As blood was pumped through the tube, urea and other low MW metabolites diffused across the membrane to the dialysate down a concentration gradient. The cellophane tubing did not allow diffusion of larger components in the blood such as proteins or blood cells, not did it remove excess water. Kolff's first tubular dialyzer required several liters of blood to prime the system – a major operational problem. Different configurations were developed to solve this problem, namely the hollow fiber, which by 1996 and up until now has more than 95% of the market [2].

The vascular access is essential for an efficient HD procedure and can assume three types: arteriovenous fistula (AVF), arteriovenous graft, and central venous catheter. AVF remains the first choice for chronic HD as it is associated with longevity and the lowest rates of morbidity and mortality [51]. As the blood flows from the patient into the circuit, through inert or highly biocompatible material, its natural disposition is to coagulate. Therefore, anticoagulation is necessary and achieved via heparin-infusion, positioned after the pump and prior to the dialyzer inlet [2,8]. Further on, the blood enters the dialyzer where solute exchange and water removal takes place, and flows back into the patient, as depicted in Figure 2-1.

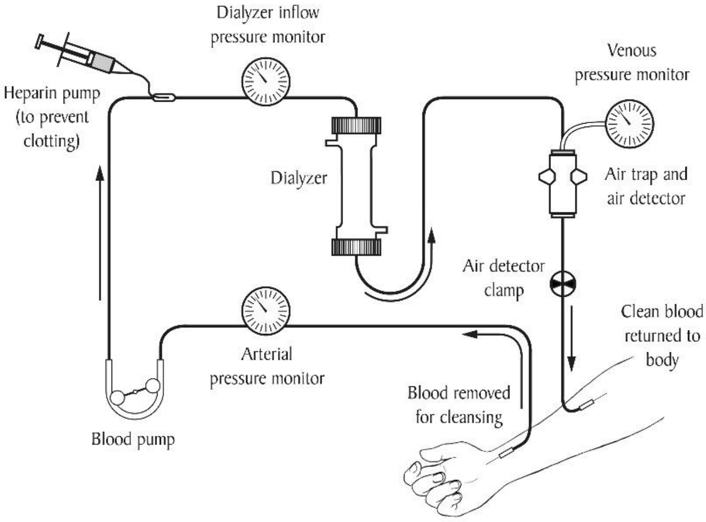

Figure 2-1. Representation of the extracorporeal blood circuit characteristic of hemodialysis. Adapted from [52].

The HD membrane is the core of the AK, as it is responsible from removing accumulated uremic toxins, excess ions, and water, while simultaneously retaining vital components from the blood of

ESRD patients, as is the case of albumin. Furthermore, HD requires membranes with high blood compatibility, selectivity and fouling resistance, for which these conditions have been satisfied through the use of synthetic membranes [50].

Hollow fiber dialyzers (Figure 2-2) lead the HD market and typically contain 0.8-2.2 m^2 of membrane in the form of fibers with 0.1-0.2 mm in diameter [8,24]. A crucial advantage of the hollow fiber design is that only 60-100 mL of blood is required to fill the dialyzer [24].

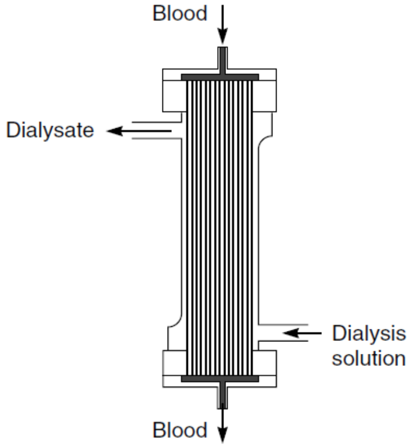

Figure 2-2. Schematic representation of a hollow fiber dialyzer and direction of blood and dialysate streams. Adapted from [24].

Through its transit in the dialyzer, the blood comes in contact with the dialysate solution, the composition of which is designed to resemble plasma, where the process of diffusion and convection are combined to achieve solute exchange and water removal across a bundle of semipermeable membranes [53]. Diffusion takes place according to a concentration gradient between the blood and dialysate compartments, and is dependent on the diffusive coefficients of the solutes and membrane properties, whereas ultrafiltration is the principle underlying convection. In the latter, transfer of fluid volumes accompanied by the removal of solutes is dependent on the UF flowrate and the solute sieving coefficient for the membrane [8].

2.2. Membranes for the artificial kidney

Traditionally, dialysis membranes have been broadly classified on the basis of their composition as cellulosic or synthetic [54]. The earliest hemodialysis membranes consisted of regenerated cellulose that rendered small pore sizes allowing clearance of molecules smaller than 5000 Da into the dialysate and was associated with an inflammatory response [54]. Although cellulose has been used successfully in hemodialyzers for many years, there is some concern about the ability of the free hydroxyl groups on the membrane surface to activate the blood clotting process. When cellulose-based dialyzers are reused, the membrane blood compatibility improves because a coating of protein has formed on the membrane surface [55]. In the early 1970s, in an attempt to enhance the hemocompatibility of regenerated cellulose membranes, researchers turned to modified cellulose materials, such as cellulose acetate (CA) and cellulose triacetate, where a large percentage of the hydroxyl groups is replaced with an acetate radical, eliminating the active surface sites for complement protein interaction. This modification also led to the improvement of solute mass transfer [56]. Also occurring in this decade was the development of synthetic membranes, such as polyacrylonitrile (PAN) and polysulfone (PS) [57]. These latter membranes differed fundamentally from cellulosic materials not only in their polymeric composition but also in a number of other features, including larger pore size, decreased thickness, and hydrophobicity. Furthermore, they are less prone to complement activation. An attractive feature of some of the new synthetic polymer membranes is their ability to remove some of the middle molecular weight metabolites in blood. Cellulose membranes efficiently remove the major metabolites, urea and creatinine, from blood, but metabolites with MWs between 1000 and 10000 Da are removed poorly. Patients on long-term dialysis are believed to accumulate these metabolites, which are associated with a number of health issues [55].

Due to their hydrophobicity, synthetic HD membranes must be rendered hydrophilic before they can be used in HD, thus adding an extra step in the preparation process. Furthermore, their final hemocompatibility and filtration performance depends on the hydrophilization processes they are subjected to [58]. In terms of pore size, those of synthetic membranes are generally larger than cellulosic membranes [54], which allows for a faster extraction of water and potential removal of middle-sized and protein bound retention solutes [59].

Due to the higher water permeability and efficiency in the removal of UTs of larger molecular weight, the majority of HD membranes on the market today are made from synthetic polymers [60]. Nevertheless, the highly porous structure of synthetic membranes has disadvantages: studies focused on the dialysate/ultrafiltrate removed from patients subjected to high-flux HD identified the convective removal of useful and even vital compounds found in blood [59,60], such as albumin and vitamin D-transporting protein [61]. At a much smaller scale, melt-spun CA membranes are being successfully used in HD [62,63], with studies reporting their low toxicity and reduced complement activation [64].

Limited chemical resistance, low mechanical strength, susceptibility to environmental degradation and limited shelf life are some of the drawbacks of cellulosic membranes [65]. To overcome these limitations, researchers have focused on the development of hybrid organic/inorganic materials which combine the rigidity and high thermal stability of the inorganic material with the flexibility, ductility and processability of CA. In this sense, this work follows the trend of synthesizing novel monophasic hybrid CA-SiO_2-$(CH_2)_3NH_2$ membranes, in which the inorganic and organic parts are covalently bonded [66].

2.2.1. Uremic syndrome and challenges of toxin removal

Uremic syndrome results from a malfunctioning of various organ systems due to the retention of compounds which, under normal conditions, would be metabolized by the kidneys and subsequently excreted into urine [67]. These biologically active compounds, also known as uremic toxins, play a prominent role in the progressive loss of kidney function in CKD patients, in addition to cardio-vascular and cerebrovascular damage due to their toxic effects [68]. Currently, over 140 UTs have been implicated in the pathogenesis of uremic syndrome [69] and are generally divided into 3 different groups, a classification proposed by the European Uremic Toxin work group (EUTox) [70], according to their molecular weight and their relative affinity for protein binding: (1) small water-soluble compounds (MW < 500 Da); (2) middle molecules (MW ≥ 500 Da); and (3) protein-bound uremic toxins (PBUTs) (MW < 500 Da when free, > 66.5 kDa when bound to albumin) [69]. The prototype compounds for these major groups are identified in Table 2-1.

Table 2-1. Different classes of uremic toxins, as proposed by the EUTox [70].

Class of molecules	MW range	Percentage of identified molecules	Prototype
Small water-soluble compounds	< 500 Da	46%	Urea (60 Da)
Middle molecules	≥ 500 Da	28%	β_2-microglobulin (11 818 Da)
Protein-bound compounds	< 500 Da, when free > 66.5 kDa, when bound to albumin	26%	Indoxyl sulfate (213 Da)

Current dialytic procedures only partially restore kidney function, as they are mainly effective in removing the small-water soluble compounds, which circulate without significant protein binding. As for the middle molecules, with relatively high MW, dialyzing through membranes with a larger pore size, the so-called high-flux membranes, may counteract the complications in standard dialysis, in which there is low to no removal of these compounds [71]. Studies have shown that high-flux membranes are reasonably efficient in removing middle molecules, whilst avoiding albumin leakage, which translates in a reduction of cardiovascular mortality by about 15% [72].

The main challenge of toxin removal is attributed to protein-bound uremic toxins, for which clearance is impaired due to their high plasma protein binding, especially to human serum albumin [73]. The concentration of bound toxins is variable and depends on the binding affinity towards plasma proteins. However, when bound to these transport proteins, accounting for the greatest PBUT fraction, they form large size protein-toxin complexes which remain essentially untouched in therapy, as they are unable to permeate through the membrane. In most cases, protein binding is reversible, as both the toxin and the protein are involved in second order noncovalent binding, such as Van der Waals forces and hydrogen bonds [74]. In fact, it is only the free fraction of the PBUT that exerts biological action and is susceptible of being metabolized [69]. Among the most problematic PBUTs, conferring renal and cardiovascular toxicity, are indoxyl sulfate and p-cresyl sulfate, which are derived from dietary amino acid metabolites by colonic microbial organisms [75].

Serum proteins have important physiological functions, which can maintain the osmotic pressure and the pH value of blood, and transport a wide variety of endogenous and exogenous compounds. Albumin is a family of globular proteins, the most common of which are the serum albumins. They are acidic, highly soluble and very stable proteins, commonly found in blood plasma, and are able to withstand temperatures of 60°C for 10h [76]. Moreover, albumin is a versatile transport protein for numerous molecules, including hormones, several important classes of drugs and endogenous toxins [74].

Bovine serum albumin (BSA) has been widely used as a model protein in various experiments for its structural homology with human serum albumin (HSA), easy preparation, high purity, and good dissolubility in water. BSA is a globular protein with dimensions of 4 nm x 4 nm x 14 nm, and its isoelectric point ranges of pH 4.0-5.0, which means that BSA molecules have the ability to be bound on the charged substances reversibly by changing the pH value [77]. It is considered as a fouling substance, since it is readily adsorbed on the surface of hydrophobic membranes [1,13].

The molecule of HSA consists of 585 amino acids forming one polypeptide chain, with a MW of 66.439 kDa. The secondary structure of the protein contains about 67% helical structures next to 33% of turn and extended chain configurations without any β-sheets [78]. The three-dimensional structure of the protein (Figure 2-3) is formed by three homologous domains (I, II and III), each consisting of two subdomains (A and B).

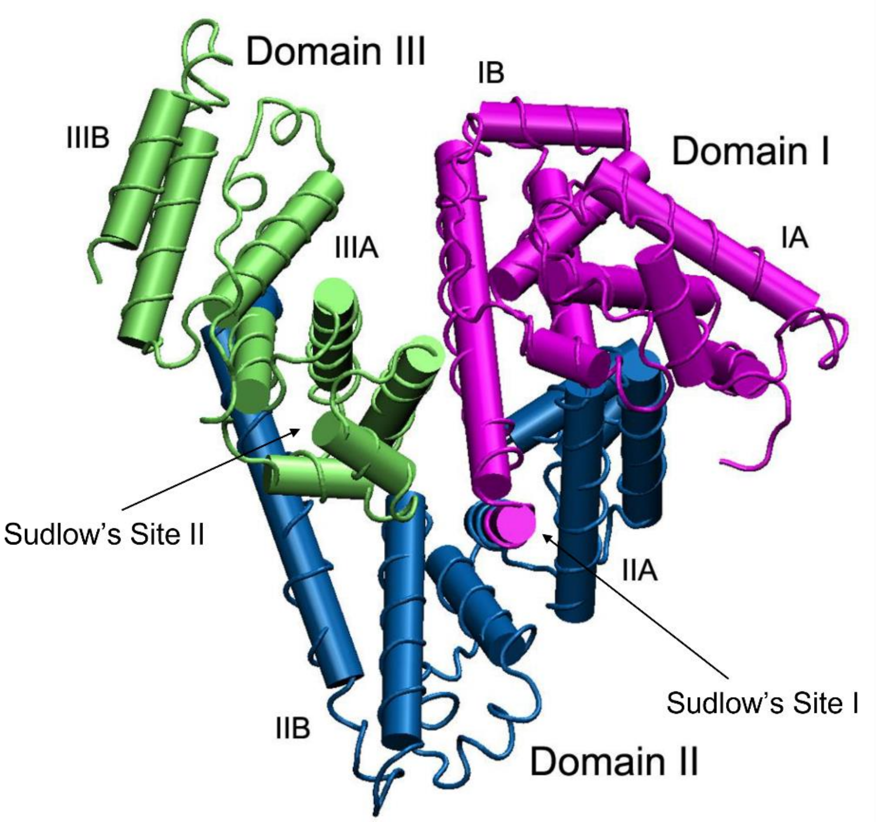

Figure 2-3. Representation of human serum albumin. Domains I, II and III are shown in purple, blue and green, respectively; each of them comprising two subdomains A and B. Also represented are α-helices, as cylinders, and ligand binding site Sudlow's site I in subdomain IIA and Sudlow's site II in subdomain IIIA. Adapted from [76].

Despite being negatively charged at physiological pH (≈ 7.40), binding sites for anionic, neutral and cationic ligands coexist on the same molecule due to regional differences in charge distribution, confirming theversatile binding capacity of albumin [74]. The primary binding sites are commonly referred to as Sudlow's sites I and II. In general, ligands that are bulky heterocyclic anions bind to Sudlow's site I, whereas Sudlow's site II ligands are aromatic and can be either neutral or bear a negative charge located peripherally on the molecule. Indoxyl sulfate and p-cresyl sulfate are reported to Sudlow's site II [69,74].

The membrane under study in this work is functionalized with amine groups, which are envisioned to translate into preferential interactions with proteins present in the blood, especially albumin, that may or may not be bound to PBUTs. The monophasic hybrid membrane is fabricated under acid conditions, giving rise to the protonation of NH_2 groups. Therefore, when in close contact with albumin, a strong electrostatic interaction between the positively charged $-\mathrm{NH}_3^+$ group from the hybrid membrane and the -COOH or -NH from albumin does occur. This electrostatic interaction may allow the displacement of PBUTs from albumin, which is guaranteed to be a breakthrough, since they are one of the main causes of comorbidities and mortality in dialysis patients, and are not yet removable in current therapies [79].

2.3. Motivation and thesis objectives

Currently, blood purification techniques focused on treating renal failure are mainly effective on removing water-soluble uremic toxins and are limited by the lack of protein-bound uremic toxins' clearance from the blood of uremic populations. The aim of this study is to evaluate the potential of monophasic hybrid CA-SiO_2-$(CH_2)_3NH_2$ asymmetric membranes for application in blood purification devices such as HD, where the preferential permeation of uremic toxins and the retention of vital blood components such as albumin are mandatory. For this, a monophasic hybrid CA-SiO_2-$(CH_2)_3NH_2$ asymmetric membrane containing 95 wt% CA and 5 wt% SiO_2 + SiO_2-$(CH_2)_3NH_2$ was synthesized and characterized in an in-house built single hemodialysis membrane module under dynamic conditions. The functionalization of the membrane with amine groups is expected to translate into interactions between the membrane and proteins, such as albumin, allowing the displacement of protein-bound uremic toxins. For comparison purposes a pure CA membrane was also synthesized and characterized. The surface and cross-section morphologies of the membranes were characterized by scanning electron microscopy and the chemical composition was analyzed by Fourier transform infrared spectroscopy in attenuated total reflection mode. Permeation experiments were carried out to evaluate the membranes performance in terms of hydraulic permeability, molecular weight cut-off and rejection coefficients to a group of small water-soluble compounds and bovine serum albumin.

3. Materials and Experimental Methods

3.1. Materials

Membranes were synthesized with cellulose acetate (CA) ($C_6H_7O_2(OH)_3$, ~30 000 g/mol, reagent grade ≥ 97%, esterification degree ~40%) from Sigma-Aldrich (Steinheim, Germany), tetraethyl orthosilicate (TEOS) ($Si(OC_2H_5)_4$, 208.33 g/mol, reagent grade 98%), purchased from Alfa Aesar (Karlsruhe, Germany), 3-(triethoxysilyl)–propylamine (APTES) ($C_9H_{23}NO_3Si$, 221.37 g/mol, reagent grade ≥ 98%) purchased from Sigma-Aldrich (Steinheim, Germany), formamide (CH_3NO, 45.02 g/mol, ≥ 99.5%) purchased from Carlo Erba (Val-de-Reuil, France), acetone (C_3H_6O, 58.08 g/mol, ≥ 99.6%) purchased from Labsolve (Zedelgem, Belgium), and nitric acid (HNO_3, 63.01 g/mol, 1.39 g/mL at 20°C, 65% v/v) purchased from LabSolve (Zedelgem, Belgium).

Membranes drying was performed with isopropanol (≥ 99.8%) from Honeywell (Seelze, Germany) and n-hexane (≥ 95%) from Carlo Erba (Val-de-Reuil, France).

Permeation experiments were carried out with urea (MW 60.06 g/mol) purchased from Merck (Darmstadt, Germany), creatinine (MW 113.12 g/mol) purchased from Sigma-Aldrich (Steinheim, Germany), uric acid (MW 168.11 g/mol) purchased from Alfa Aesar (Kandel, Germany) and bovine serum albumin (BSA) (MW 66.5 g/mol) purchased from Sigma-Aldrich (Steinheim, Germany).

MWCO was studied using polyethylene glycol (PEG) 400 (MW 400 g/mol) purchased from Sigma-Aldrich (Steinheim, Germany), PEG 3000 (MW 3000 g/mol), PEG 6000 (MW 6000 g/mol), PEG 10000 (MW 10000 g/mol) purchased from Merck (Hohenbrunn, Germany), PEG 20000 (MW 20000 g/mol) purchased from Sigma-Aldrich (Steinheim, Germany) and PEG 35 000 (MW 35 000 g/mol) purchased from Merck (Hohenbrunn, Germany).

Phosphate buffer saline used to dissolve BSA was prepared using sodium chloride (NaCl, 58.44 g/mol, ≥ 99.5%) purchased from Merck (Darmstadt, Germany), potassium chloride (KCl, 74.56 g/mol, ≥ 99.5%) purchased from Panreac (Barcelona, Spain), potassium dihydrogen phosphate (KH_2PO_4, 136.09 g/mol, ≥ 99.5%) purchased from Merck (Darmstadt, Germany) and disodium hydrogen phosphate dihydrate ($Na_2HPO_4.2H_2O$, 177.99 g/mol, ≥ 99.5%) purchased from Merck (Darmstadt, Germany).

Quantification of BSA was carried out according to the Bradford protein assay. Bradford reagent was prepared using Coomassie Brilliant Blue G-250 ($C_{47}H_{48}N_3NaO_7S_2$, 854.04 g/mol) purchased from Panreac (Barcelona, Spain), ethanol (C_2H_6O, 46.07 g/mol, 96% v/v) purchased from Manuel Vieira & C^a (Torres Novas, Portugal) and phosphoric acid (H_3PO_4, 98.00 g/mol, 1.71 g/mL at 20°C, reagent grade 85%) purchased from Honeywell (Seelze, Germany).

All chemicals used in the synthesis, drying and characterization of the monophasic membranes were used without further purification.

3.2. Membrane synthesis

The monophasic hybrid integrally skinned asymmetric $CA\text{-}SiO_2\text{-}(CH_2)_3NH_2$ membrane was prepared by coupling of the phase inversion method and sol–gel technique. The monomers that take part in the sol-gel reactions are represented in Figure 3-1.

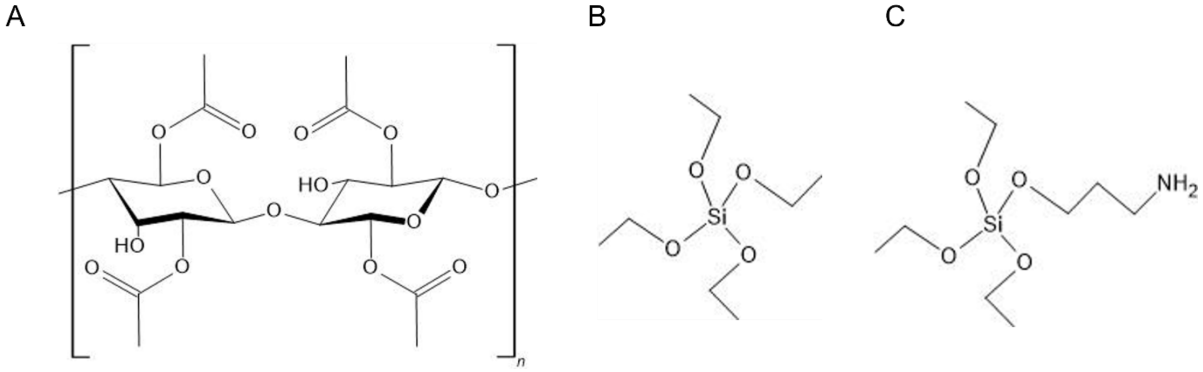

Figure 3-1. Cellulose-acetate structure (**A**) and sol-gel silica precursors: TEOS (**B**) and APTES (**B**).

Functional groups play a significant role in directing and controlling organic reactions, in introducing design surface properties or in tuning mechanical performance. Amine-functionalization of the membrane through the use of APTES aims on taking advantage of the amine chemical versatility and high reactivity, due to its alkaline and nucleophilic character [76]. Chemical interaction between the amino groups of the membrane and carboxyl and/or secondary amine groups of BSA play the dominant role in BSA adsorption to the membrane surface [77].

The introduction of silica and subsequent formation of complex C-O-Si 3D networks is expected to enhance membrane selectivity and permeation properties, along with antifouling properties and mechanical stability, overcoming the limitations associated to pristine CA membranes [66,80].

The use of acetone as a solvent for cellulose acetate provides proper viscosity to the casting solution. In case the ratio of acetone to cellulose acetate was too low, very viscous casting solutions would result and could not be used to cast uniform films. Conversely, an overly high ratio would yield thin films which would become gelatinous upon immersion [81].

The role of formamide is essentially of pore promoter since it is not a true solvent for cellulose acetate [14,82]. In fact, formamide may be classified as a swelling agent [27,83] such that when cellulose acetate is exposed to it, the polymer swells as a result of the increase in the total volume of the polymer-liquid system. Furthermore, it increases the solvent power of acetone [27]. Given this, during exposure to air the more volatile solvent – acetone – evaporates from the cast film and the solution is brought to the point of polymer precipitation [14].

The casting solution of the monophasic hybrid $CA\text{-}SiO_2\text{-}(CH_2)_3NH_2$ membrane was prepared in two steps. Firstly, cellulose acetate, formamide and acetone were mixed in the reaction vessel to allow complete dissolution of cellulose acetate. Thereafter a 5h period of mixing, TEOS, APTES (to uphold amine in situ functionalization) and nitric acid (as a catalyst) were added to the previous solution, promoting sol-gel hydrolysis and simultaneous or sequential hetero-condensation. The final solution was left on an agitation plate for another 19h, resulting in a total homogenization time of 24h.

Similarly to the hybrid membrane, a reference casting solution of the pristine CA membrane was prepared by mixing cellulose acetate, formamide and acetone for a period of 24h. The compositions of both membranes, on weight basis, are represented in Table 3-1.

Table 3-1. Casting solution compositions, on weight basis.

	Casting solution composition	
	CA-SiO_2-$(CH_2)_3NH_2$	**CA**
Cellulose Acetate	16.40	17.00
Formamide	29.00	30.00
Acetone	51.10	53.00
TEOS	2.40	-
APTES	0.64	-
Nitric acid	12 drops	-

The addition of nitric acid provides the acidic environment necessary to catalyze sol-gel hydrolysis and hetero-condensation reactions. When these occur at pH ~3, above the isoelectric point of SiO_2, the condensation rate is proportional to the concentration of hydroxide groups and the following reactions take place:

$$\equiv\text{Si-OH} + \text{OH}^- \xrightarrow{\text{fast}} \equiv\text{Si-O}^- + \text{H}_2\text{O} \tag{3-1}$$

$$\equiv\text{Si-O}^- + \text{HO-Si} \xrightarrow{\text{slow}} \equiv\text{Si-O-Si}\equiv + \text{OH}^- \tag{3-2}$$

In these conditions, complete hydrolysis is achieved by nucleophilic attack, producing linear or highly branched polymeric species, with a continuous 3D fractal structure with nanopore diameters (< 2 nm) [84]. The subsequent homo-condensation step can occur between silanol groups from the inorganic phase originating inorganic nano/micro domains (Equation 3-2). Moreover, hetero-condensation between Si-OH groups from the inorganic phase and the C-OH groups from the polymer phase (Equation 2-3) may also occur, with formation of Si-O-C bonds (Equation 3-3: top and bottom products, respectively). The new hybrid casting solution is then cast to form a monophasic hybrid membrane, based on carbon, silica, and amine chemical species, originating complex carbon-silica networks.

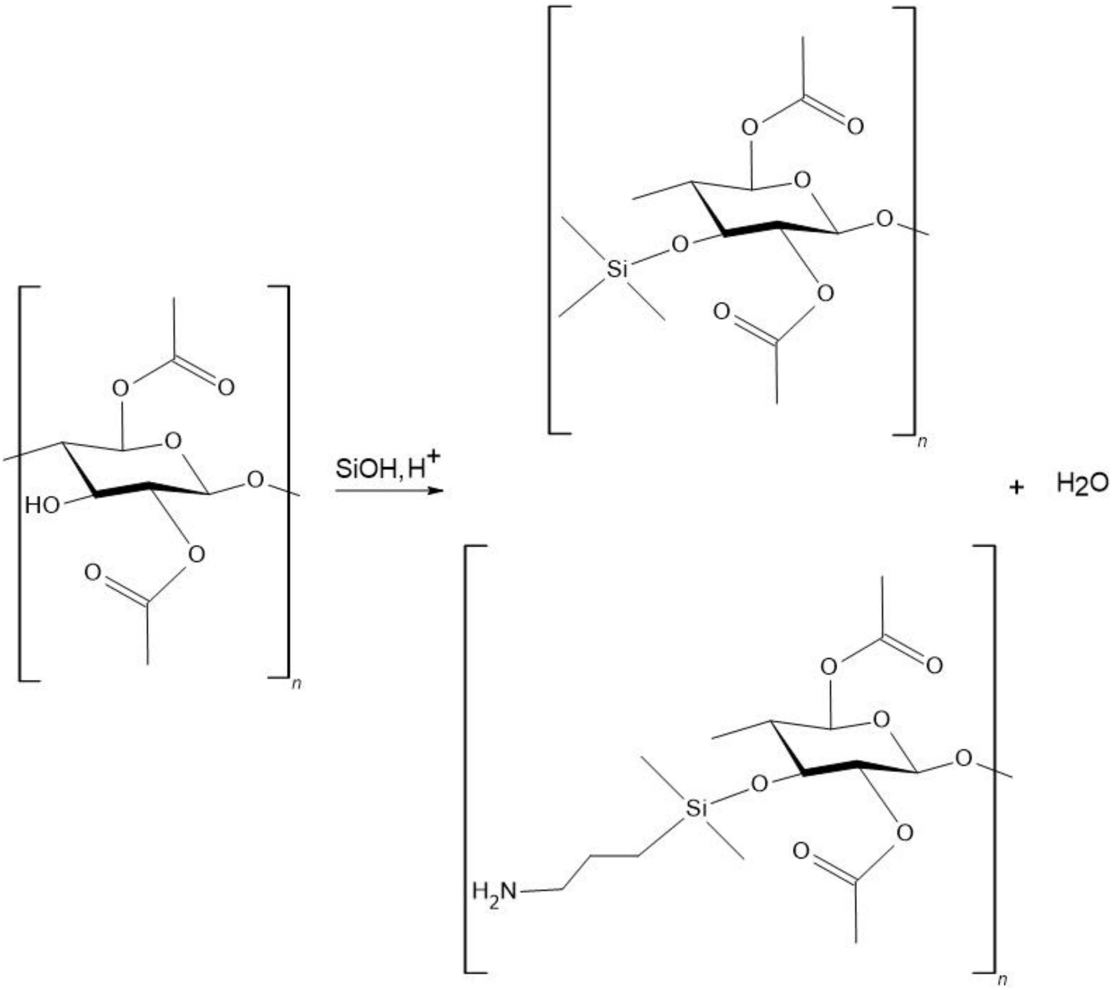

(3-3)

Prior to the casting, the glass plates as well as the casting knife were cleaned with acetone to ensure any impurities or polymer residues from past castings are eliminated. A 250 µm Gardner knife is then placed on the edge of the glass plate surface, where the casting solution will be distributed, and displaced at a constant velocity towards the opposite edge of the glass plate surface. Thereafter a solvent evaporation time of 30s, the film over the glass plate is immersed in the coagulation bath containing iced water at a temperature of 4 ± 1 °C. After a residence time of approximately 3h in the coagulation bath, the CA and CA-SiO_2-$(CH_2)_3NH_2$ membranes were detached from the glass plate and stored separately in deionized water at 4 ± 1 °C. The membrane composition is evidenced in Table 3-2.

Table 3-2. Hybrid membrane composition, on molar basis.

	Membrane composition
	CA-SiO_2-$(CH_2)_3NH_2$
Cellulose Acetate	0.031
SiO_2	0.660
$SiO_{1.5}$-$(CH_2)_3NH_2$	0.166
SiO_2 + $SiO_{1.5}$-$(CH_2)_3NH_2$	0.826
Non-functionalized SiO_2 / Total SiO_2 (i.e. TEOS / TEOS + APTES)	80
Amine functionalized silica / Total SiO_2 (i.e. APTES / TEOS + APTES)	20

3.3. Membrane drying process

Preservation of membrane properties in terms of pore size and pore distribution is imperative upon characterization and storage, and can be achieved with the adequate drying procedure.

Membranes obtained via the phase separation process using water as the precipitating agent, normally have a higher water content than membranes produced by other procedures, such as solvent evaporation [85]. Direct water evaporation will cause the microporous membrane structure to collapse and form a denser active surface layer, contributing to the loss of permeation performance. In this regard, several drying methods have been introduced, such as vacuum drying, freeze drying and solvent exchange [86].

In the multi-stage solvent exchange technique, the water in the membrane is replaced by a water-miscible first solvent that is a nonsolvent for the membrane material. Thereafter, the first solvent is replaced by a second solvent that is volatile. The latter is subsequently air evaporated to obtain the dry membrane [22].

Replacing water, which was a high surface tension, by another solvent with a much lower surface tension reduces the capillary forces acting during drying, avoiding pore collapse [12]. The choice of the solvent will depend on the membrane material since it must be a non-solvent for the membrane.

In this study, the employed drying method was adapted from Lui et. al. [87], using deionized water, isopropanol as the first solvent, and n-hexane as the second solvent. The dry membrane is achieved by immersion in each solvent solution of successively higher contents (25, 50, 75 and 100% V/V) for a period of 24h at room temperature. The last stage of the drying process takes place in a desiccator, to ensure complete evaporation of the second solvent.

3.4. Membrane characterization

3.4.1. Scanning electron microscopy (SEM)

Prior to being imaged by scanning electron microscopy (SEM), the CA and CA-SiO_2-$(CH_2)_3NH_2$ membranes were submitted to the drying process described in section 3.3. Samples of both membranes were then fractured in liquid nitrogen, mounted on a stub and sputter-coated with gold. Micrographs of the top dense surface (magnification: 1000x), cross-sections (magnification: 700x) and of the porous bottom layer (magnification: 4000x) were obtained. The active layer and total thickness of the membranes was calculated using the ImageJ software (version 1.53k, from National Institutes of Health). For each membrane, three randomly selected zones from the entire active layer and cross-section images were measured and the mean thickness and standard deviation were calculated. In order to determine the average pore size of the porous bottom layer, the images were binarized using a threshold adjustment and subsequently analyzed via the Measure tool.

3.4.2. Attenuated total reflection-Fourier transform infrared (ATR-FTIR) spectroscopy

Attenuated total reflection-Fourier transform infrared spectroscopy (ATR-FTIR) was used to analyze the chemical composition of the active layer surfaces of samples of the dried CA and CA-SiO_2-$(CH_2)_3NH_2$ membranes. Infrared spectra of the samples with the active layer facing upwards, were obtained with a PerkinElmer Frontier FT-IR spectrometer (940 Winter Street, Waltham, MA 02451, USA), using a Pike Miracle Single Reflection ATR sampling accessory from Pike Technologies, with a Ge crystal (Graseby Specac, Smyrna; sampling depth: 0.2-1.1 μm at 4000-650 cm^{-1}). Each spectrum was obtained by averaging 256 scans with a resolution of 4 cm^{-1}. Infrared spectra received were reported as percentage transmittance values as a function of the number of waves.

3.5. Experimental setup

3.5.1. Single hemodialysis membrane module (SHDMM)

A single hemodialysis membrane module (SHDMM) was custom-made by the micromachining of acrylic plates. Figure 3-2 shows the schematic representation and dimensions of the five units that compose the SHDMM. Unit II defines the feed flow chamber while the purpose of the perforated piece, unit III, is to support the membrane. Unit IV defines the chamber in which the permeate is collected and units I and V seal the top feed flow and bottom permeate collecting chambers, respectively. The membrane is placed with its active layer facing upwards on top of unit III, with a filter paper beneath it, to prevent damage to the membrane when all units are sealed together by means of stainless-steel screws. Because of the large thickness of unit III (1 cm), on top of which the membrane is placed, the solutions in the feed flow channel and the permeate compartment do not interact close enough to establish a concentration gradient. Therefore, the solute diffusion between the compartments is negligible and it is assumed that fluid and solute removal occur exclusively by convection. The feed flow and permeate collecting chambers were designed to be slit-like microchannels, where the channel height (2B) is much smaller than the other two dimensions: width (W) and length (L). As such, the dimensions of the microchannels are 2B = 0.3 cm, W = 3.0 cm, and L = 25.0 cm (2B ≪ W and L). The effective membrane surface area was assessed and found to be defined by the area of the membrane clamped between the O-ring that seals units I and II, assuming a value of 105 cm^2.

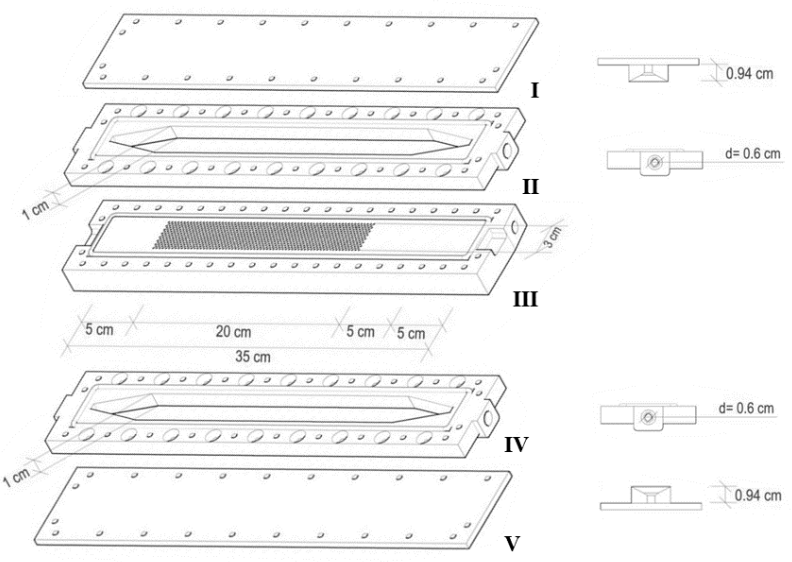

Figure 3-2. Schematic representation of the single hemodialysis membrane module (SHDMM). Unit I seals the feed flow chamber, represented by unit II. Unit V seals the permeate collecting chamber, represented by unit IV. Unit III is the supporting surface for the membrane to be tested.

The height of the feed flow channel is a relevant parameter when assessing fouling events. During permeation experiments, the channel height may vary due to the deposition of molecules on top of the membrane. In such cases, there should be a significant increase in the pressure drop, ΔP, across the feed flow channel, leading to the reduction of the microchannel height.

After the membrane and filter paper have been assembled inside the SMHM the feed channel height is estimated taking into account the data depicted in Figure 3-3.

Considering the open channel of unit II depicted in Figure 3-2 as a plane narrow slit, formed by two flat parallel walls that are a distance 2B apart, such that B ≪ W < L. The fluid flow is in the z-direction, such that the velocity vector is of the form $\vec{\mathrm{v}} = (0{,}0{,}\mathrm{v_z})$ and $\mathrm{v_z}$ is a function only for x.

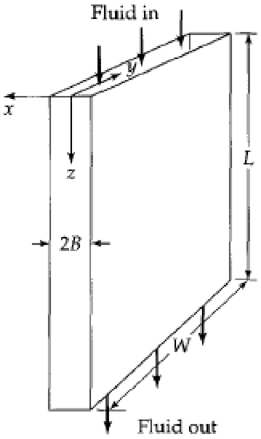

Figure 3-3. Fluid flow in a narrow plane slit. Adapted from [88].

The velocity profile can be obtained by integrating the expression resulting from the application of a differential momentum balance, at steady-state, to a slit of thickness Δx. Furthermore, the velocity distribution for laminar, incompressible flow of a Newtonian fluid in a plane narrow slit is parabolic, such that the maximum velocity occurs at $x = 0$ (Figure 3-3). Therefore,

$$v_{z,\,max} = \frac{\Delta P B^2}{2 \mu L} \tag{3-4}$$

where $v_{z,max}$ is the maximum velocity, ΔP is the difference in pressure between the inlet and outlet, B is the half-height of the microchannel, μ is the viscosity of the fluid and L is the length of the slit.

The mass flowrate is further obtained by integrating the velocity profile over the cross section of the slit, considering the average velocity as $v_{z,avg} = \frac{2}{3} v_{z,max}$, such that

$$\dot{m} = \frac{2}{3} \frac{\Delta P B^3 \rho W}{\mu L} \tag{3-5}$$

where $\dot{m}$ is the mass flowrate, ρ is the density of the fluid and W is the width of the slit.

The half-height of the microchannel is obtained by rearrangement of Equation 3-5, which is analogous to the Hagen-Poiseuille law for circular tubes, and describes the fully-developed laminar flow of a Newtonian fluid in a narrow slit [88]:

$$B = \sqrt[3]{\frac{3}{2} \frac{\mu L}{W} \frac{Q_F}{\Delta P}} \tag{3-6}$$

where Q_F is the feed flowrate.

3.5.2. Feed circulation circuit

Figure 3-4 represents the circuit that simulates the extracorporeal blood circulation circuit found in HD machines. The feed reservoir, a 500 mL glass Kitasato, is placed in a thermostatically controlled water bath (model CORIO C, from JULABO, Seelbach, Germany) to maintain the feed solution at the average normal body temperature, 37°C. The feed solution is pumped from the reservoir and through the circuit by a peristaltic pump similar to the ones used in extracorporeal circulation such as dialysis (model ECOLINE VC-360, from ISMATEC, Wertheim, Germany) and its pulsation effect is attenuated by a damper, allowing the feed fluid to enter the SHDMM at a constant pressure. The ultrafiltrate is collected in the permeate collecting chamber and the fraction of the feed solution that has not permeated is recirculated back to the feed reservoir. A three-way valve placed midway between the outlet and the reservoir enables the collection of feed samples. Throughout the entire circuit, polyvinyl chloride (PVC) tubing (Tygon Saint-Gobain, La Defense, Courbevoie, France) with an inner diameter of 3 mm and Shore hardness of 55A was used to ensure that the shedding of particles from the interior of the tubing, a phenomenon known as spallation [89,90], is low.

Four medical grade pressure sensors (Deltran® Utah Medical Products, Inc., Midvale, UT, USA) - P1, P2, P3 and P4 - register the pressure at crucial points of the circuit. P1 and P2 register the pressure at the inlet and outlet of the feed flow chamber, respectively, whereas P3 and P4 register the pressure at the inlet and outlet of the permeate collecting chamber, respectively. The pressure sensors are connected to a data acquisition card (National Instruments cDAQ-9172, USA) which records the pressure variations throughout time via a LabView module (National Instruments, 9237, Austin, TX, USA). The cross on the left to the sensor represented by P3 indicates that the tube is clamped and therefore the ultrafiltrate is collected by the tube placed after P4.

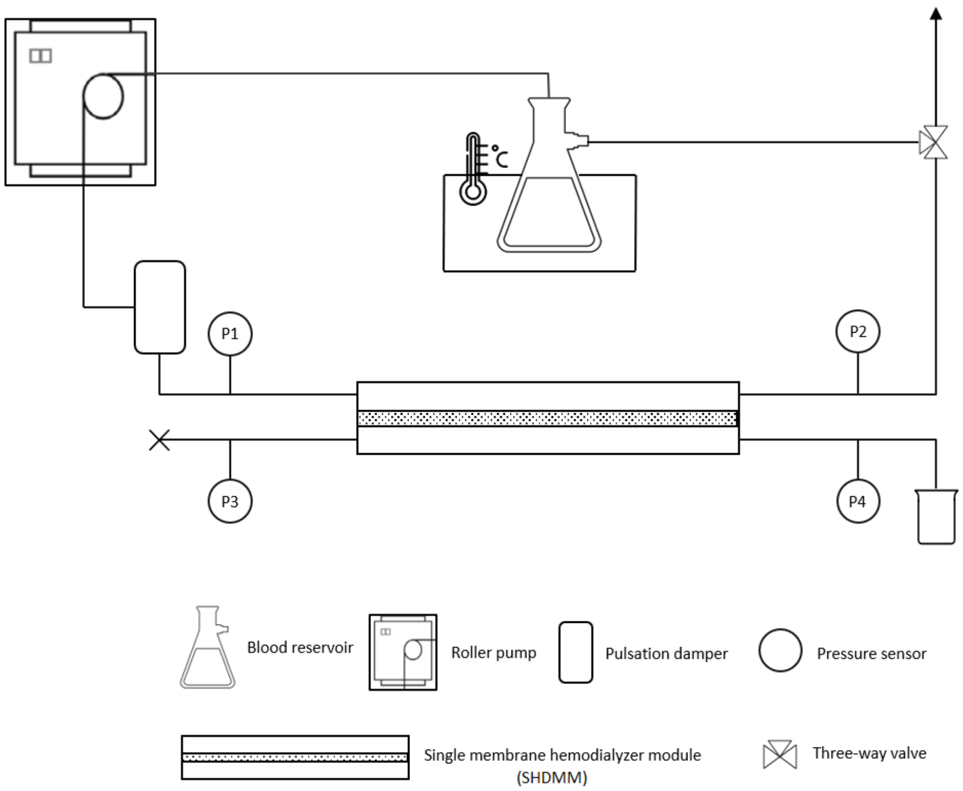
P1
P2
P3
P4
°C
Blood reservoir
Roller pump
Pulsation damper
Pressure sensor
Single membrane hemodialyzer module (SHDMM)
Three-way valve

Figure 3-4. Schematic representation of the experimental setup used for permeation experiments under dynamic conditions.

3.5.3. Characterization of the SHDMM: pressure profile, pressure drop, transmembrane pressure, microchannel height, shear rate and shear stress at the wall

To characterize the SHDMM, a permeation experiment was performed to obtain a typical pressure profile for the flow of deionized (DI) water at different feed volumetric flow rates (Q_F) through the SHDMM: 49 mL/min, 66 mL/min, 82 mL/min, 99 mL/min, 115 mL/min, 132 mL/min ad 148 mL/min. Figure 3-5 shows the pressure profile of the system registered continuously throughout the experiment. Pressures P1 and P2 represent the pressures at the inlet and outlet of the feed flow channel, respectively. P3 and P4 show the registered pressures at the inlet and outlet of the permeate collecting chamber. Each plateau represents the pressure registered for each pressure sensor resulting from the Q_F imposed by the peristaltic pump.

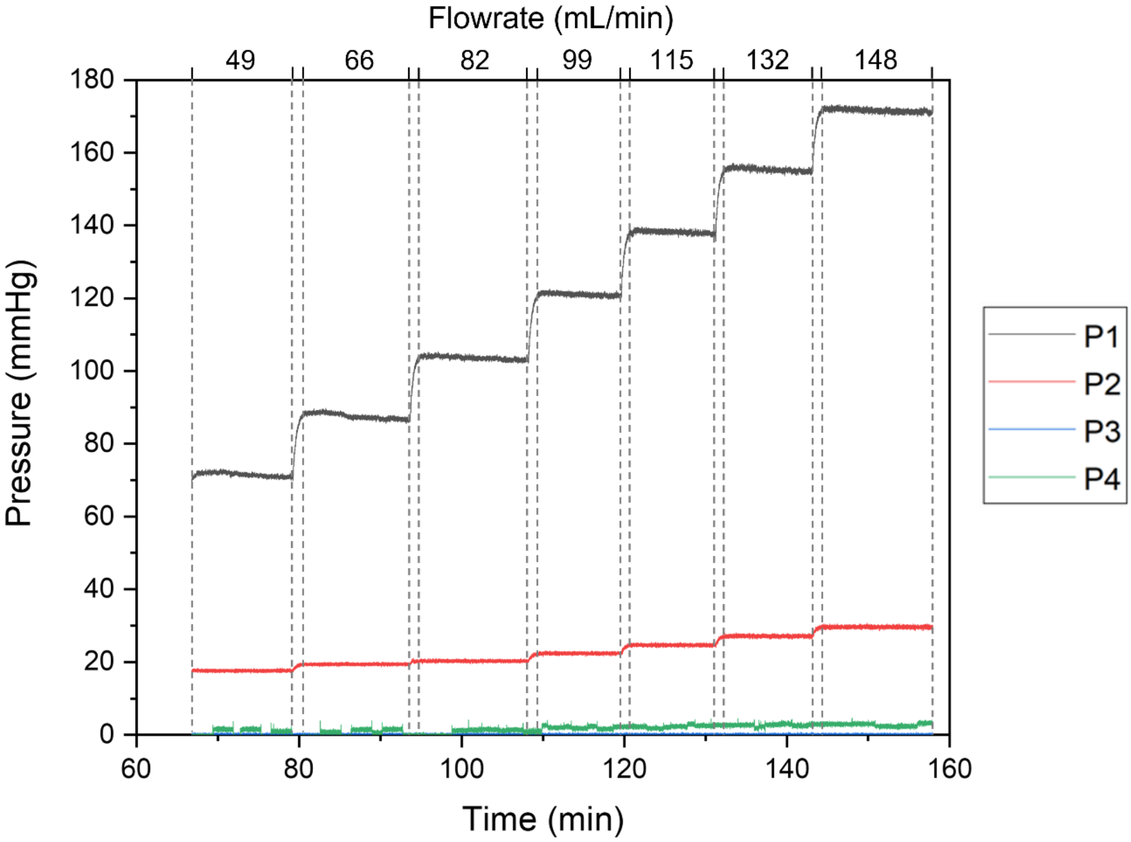

Figure 3-5. Pressure profile of the circuit during the circulation of DI water through the SHDMM circuit at different values of Q_F, which are delimited by the dashed lines. The pressure data is colour-coded according to the different sensors: black line P1, red line P2, green line P3, and dark blue line P4.

The pressure drop (ΔP) across the feed flow channel is defined by

$$\Delta P = P_1 - P_2 \tag{3-7}$$

The transmembrane pressure (TMP) is the hydrostatic pressure gradient between the feed flow chamber and permeate collecting compartment, acting as the driving force for solute removal, and has unique values along the length of the membrane [34]. Assuming a linear variation of fluid pressure with axial distance along the channel, TMP is defined by

$$\mathrm{TMP} = \frac{P_1 + P_2}{2} - \frac{P_3 + P_4}{2} \tag{3-8}$$

As mentioned in section 3.5.1, the feed flow microchannel has a slit-like geometry where the channel height (2B = 0.3 cm) is much smaller than the other two dimensions: width (W= 3.0 cm) and length (L = 25.0 cm). When the membrane is placed inside the SHDMM, the height of the feed flow microchannel is no longer 0.3 cm and must be accurately calculated (Equation 3-6).

The shear stress exerted at the flow boundaries, or walls of the microchannel, τ, can be calculated by balancing the shear force at the wall against the pressure gradient for a slit channel [88]:

$$\tau = \frac{3\mu Q_F}{2B^2W} \tag{3-9}$$

Shear rates, γ, at the wall are found by dividing the shear stress by the viscosity:

$$\gamma = \frac{\tau}{\mu} = \frac{3Q_F}{2B^2W} \tag{3-10}$$

Shear rates and shear stress in the device were varied from 4000 to 11800 s^{-1}, and to 3 and 8 Pa, respectively.

3.6. Permeation experiments under dynamic conditions

3.6.1. Water permeability

Permeation experiments were performed in the circuit containing the SHDMM to characterize the monophasic hybrid CA-SiO_2-$(CH_2)_3NH_2$ and pure CA membranes in terms of pure water permeability (L_P). This characteristic, also commonly referred to as ultrafiltration coefficient (K_{UF}) in dialysis, is defined as the volume of ultrafiltrate produced per hour per mmHg of transmembrane pressure [8,91]. It is most directly influenced by the membrane mean pore size, which in turn influences the solute sieving coefficient and molecular weight cut-off – both being the most important determinants of convective solute removal [91,92]. In this sense, convective therapies such as HF or HDF require high-flux membranes, offering high hydraulic permeabilities (> 20 $mL.h^{-1}.m^{-2}.mmHg^{-1}$) and high middle-molecule clearance, with transport maximized for larger solutes [48,93]. In opposition, low-flux membranes present lower hydraulic permeabilities (4-8 $mL.h^{-1}.m^{-2}.mmHg^{-1}$) and effectively remove small solutes through diffusion, but only negligible amounts of middle-sized molecules, which are considered to be more toxic and more difficult to remove by diffusion [93,94].

In order to assess the hydraulic permeability, three parameters must be established, namely the ultrafiltration flux, the transmembrane pressure, and the membrane permeation area.

Ultrafiltration flux, J, is defined as the amount of permeate produced per unit area of membrane surface per unit of time:

$$J = \frac{V}{A \times t} \tag{3-11}$$

where V is the volume of permeate, A is the membrane permeation area and t is the measuring time.

The water permeability, L_P, is obtained by the slope of the straight line obtained when J is represented as a function of TMP:

$$L_P = \frac{J}{TMP} \tag{3-12}$$

The range of the TMP used was 45, 53, 61, 71, 80, 90 and 100 mm Hg, corresponding to Q_F values of 49, 66, 82, 99, 115, 132 and 148 mL/min, respectively.

The feed temperature was kept at 37 °C, equivalent to the normal body temperature of a healthy adult, for all the permeation experiments. For comparison purposes to other membranes on the market, the water permeability found at 37 °C for the CA-SiO_2-$(CH_2)_3NH_2$ and pure CA membranes was standardized for a temperature of 25 °C by the following equations [95,96]:

$$\ln \mu = -6.78 + \frac{1983}{T} \ (r=0.99923) \tag{3-13}$$

Equation 3-13 can be written in terms of mass flux and assumes the following form, when solved for J_m:

$$J_m = \rho \frac{L_P}{\mu} \Delta P \tag{3-14}$$

As neither L_P nor ΔP are temperature-dependent, the previous expression can be rewritten as:

$$\frac{J_m(T)\ \mu(T)}{\rho(T)} = L_P\ \Delta P \tag{3-15}$$

Ultimately, the relationship between two fluxes, $J_{m,1}$ and $J_{m,2}$, at different temperatures, T_1 and T_2, respectively, is given by:

$$\frac{J_{m,1}\mu_1}{\rho_1} = \frac{J_{m,2}\mu_2}{\rho_2} \tag{3-16}$$

3.6.2. Molecular weight cut-off (MWCO)

The molecular weight cut-off (MWCO) has emerged as one of the most useful tools for characterizing UF membranes and is defined as the molecular weight at which 90% of the solute is rejected by the membrane [12]. Standard chemicals such as polyethylene glycol (PEG) are commonly used in MWCO determination [97]. Nonetheless, this definition is not absolute, and some limiting factors must be taken into account. For instance, most UF membranes are hydrophobic and tend to adsorb proteins on the surface or inside the pores due to membrane-protein interaction, jeopardizing MWCO determination and compromising membrane performance. Another example is the difficulty inherent to the selection of the marker protein used in the rejection experiment, since polymers of the same molar mass have different molecular sizes, e.g., a linear, flexible polymer is readily permeated through the membrane, whereas a globular protein of the same molecular mass will most likely be retained [1,98]. However, it is a useful tool for pre-screening and selecting UF membranes for a particular application, as it can be a simple, despite rough, indicator of rejection performance.

To determine the MWCO of each membrane, a retention curve was constructed by measuring the rejection coefficient, R, to various polyethylene glycols with increasing molecular weights (MWs) of 400 Da, 3000 Da, 6000 Da, 10000 Da, 20000 Da and 35000 Da, respectively. The increasing MW order was purposely adopted, since a 90% rejection could be obtained with a lower MW than the highest established. The rejection coefficient, R, is defined by

$$R = \frac{C_F - C_P}{C_F} \tag{3-17}$$

where C_P corresponds to the concentration of the permeate at t = 60 mins and C_F corresponds to the initial feed solution concentration. The initial concentration of the feed solutions of each solute was 485 ± 76 ppm and the permeation studies were performed for 1 hour at a Q_F of 100 ± 5 mL/min and a TMP of 76 ± 1 mmHg. Solute concentrations were determined in the permeate, initial feed and final feed samples using a total organic carbon analyzer (TOC-VCPH/CPN, Shimadzu, Japan).

The total organic carbon (TOC) of feed and permeate samples was calculated according to calibration curves for different PEGs (Appendix B). Prior to analysis, the PEG salts were dried to constant weight in the oven for 30 min, to remove water molecules from the solute. Summarily, the samples are burned in a combustion tube and the TOC components of the sample are converted into CO_2. To avoid contamination from diffusion of CO_2 from the air into the sample, samples were collected in glass vials of approximately 19 mL, which were completely filled with solution and sealed with parafilm. A carrier gas delivers the sample combustion products to a non-dispersive infrared gas analyzer (NDIR), where CO_2 is detected. The NDIR outputs an analogue detection signal that forms a peak, where its area is proportional to the TOC concentration of the sample.

For the CA-SiO_2-$(CH_2)_3NH_2$ and pure CA membranes, two plots were made on the same graph: 1) R as a function of the solute MW with the intersection of the horizontal line at R = 90%, and 2) a plot of the linearization of R, $\log\left(\frac{R}{1-R}\right)$, as a function of solute MW with the intersection of the horizontal (dashed) line at $\log\left(\frac{R}{1-R}\right) = 0.95$.

3.6.3. Rejection coefficients to low-molecular weight water soluble uremic toxins

The rejection coefficients, R, of the CA-SiO_2-$(CH_2)_3NH_2$ and pure CA membranes to markers for low-molecular weight water-soluble UTs: urea, creatinine, and uric acid, were determined by Equation 3-17. The initial feed solutions of each solute were prepared according to the highest reported concentrations of urea [70], creatinine [70], and uric acid [99]: 4.6 g/L, 240 mg/L and 83 mg/L, respectively. The permeation studies were performed for 1.5 hours at a Q_F of 100 ± 5 mL/min and TMP of 44 ± 1 mmHg. Solute concentrations were determined in the permeate and feed samples using a UV-Vis spectrophotometer (UV-1700 PharmaSpec, Shimadzu, Japan), according to each toxin wavelength of maximum absorbance, λmax: 200, 230 and 293 nm for urea [100], creatinine [101], and uric acid [102], respectively. For this, calibration curves were constructed for each toxin (4.3.4.Appendix C), which correlate the absorbance to toxin solutions of known concentrations. Feed and permeate samples were diluted to a factor of 20 for determination of urea and creatinine concentration, using 150 µL of sample to 2.85 mL of DI water. A factor of 10 was used to dilute samples for determination of uric acid concentration, consisting of 300 µL to 2.7 mL of DI water.

3.6.4. Bovine serum albumin filtration

The rejection coefficients, R, of the CA-SiO_2-$(CH_2)_3NH_2$ and pure CA membranes to BSA were determined by Equation 3-17. BSA was dissolved in PBS, that assures maintenance of a pH of 7.4. The initial concentration of the feed solutions was 884 ± 4 mg/L, and the permeation studies were performed for 450 min at a Q_F of 100 ± 5 of mL/min and TMP of 52 ± 5 mmHg. Solute concentrations were determined in the permeate, initial feed and final feed samples through the Bradford assay using a UV-Vis spectrophotometer (UV-1700 PharmaSpec, Shimadzu, Japan). Specifically, the absorbance of feed samples was measured at 595 nm, following the Bradford assay [103], whereas the absorbance of permeate samples was simultaneously measured at 590 nm and 450 nm according to a modified Bradford assay [104], allowing the determination of lower BSA concentrations.

Concentration of samples following the Bradford assay consisted of 180 µL of feed sample and 2820 µL of Bradford reagent; similarly, the blank solution contained 180 µL of DI water and 2820 µL of Bradford reagent. Concentration of samples following the modified Bradford assay consisted of 0.6 mL of permeate sample and 2.4 mL of Bradford reagent, while the blank solution contained 3 mL of DI water.

4. Results and Discussion

4.1. Membrane characterization

4.1.1. Scanning electron microscopy (SEM)

Figure 4-1 shows the SEM micrographs obtained for the active layer surface, cross-section, and bottom porous surface of the dried CA-SiO_2-$(CH_2)_3NH_2$ and CA membranes. The active layer of the membranes (Figure 4-1 A, B) is responsible for the membrane selectivity, and both exhibit completely dense active layers with no visible pores at a magnification of 1000x. The cross-section images (Figure 4-1 C, D) confirm the presence of a very thin skin layer of < 1 µm for both membranes, outlining a much thicker, porous substructure. The overall membrane thickness of the membranes was obtained from the cross-section images, yielding 103 ± 1 µm and 53 ± 1 µm for the CA-SiO_2-$(CH_2)_3NH_2$ and CA membranes, respectively. These results suggest that the introduction of silanol groups from the inorganic (TEOS) or hybrid (APTES) phases leads to membranes with increased thickness when compared to CA membranes, as previously reported [65,80], which may play an active role in the hydraulic permeability, as well as chemical and mechanical performance.

The porous structure (Figure 4-1 E, F) confers mechanical strength to the membranes, while offering little or no resistance to the permeation of water and solutes. The average pore diameter in the porous surface for the hybrid and CA membranes is 113 nm and 84 nm, respectively.

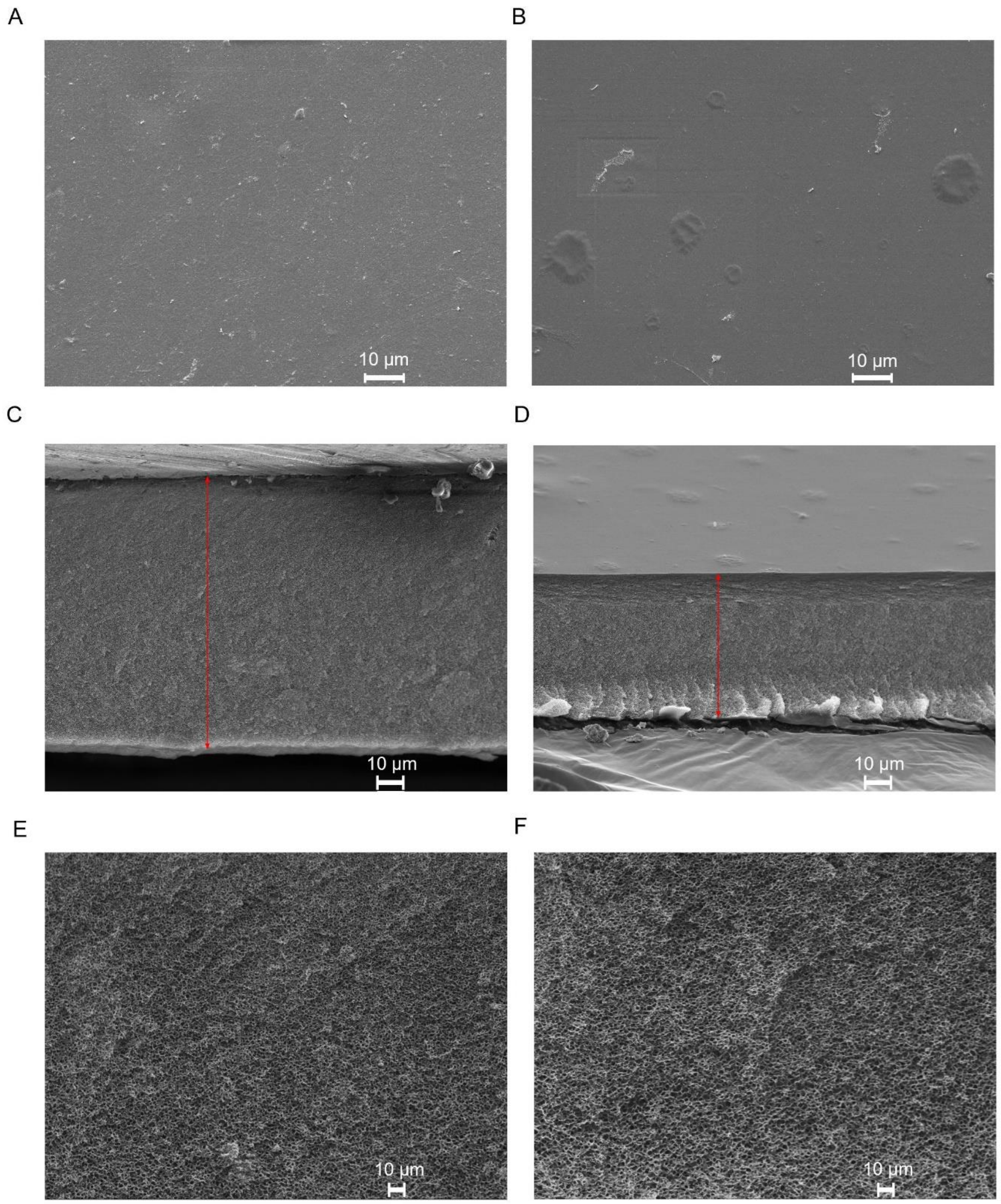
A
B
10 μm
10 μm
C
D
10 μm
10 μm
E
F
10 μm
10 μm

Figure 4-1. SEM images of the CA-SiO$_2$-(CH$_2$)$_3$NH$_2$ (**A**, **C** and **E**) and CA (**B**, **D** and **F**) membranes. **A**, **B**: top active layer (×1000). **C**, **D**: cross-section (×700) where the red lines indicate the membranes' thickness. **E**, **F**: bottom porous surface (×4000).

4.1.2. Attenuated total reflection-Fourier transform infrared spectroscopy (ATR-FTIR)

The ATR-FTIR spectra of the active layer of the CA-SiO_2-$(CH_2)_3NH_2$ and CA membranes are compared in Figure 4-2.

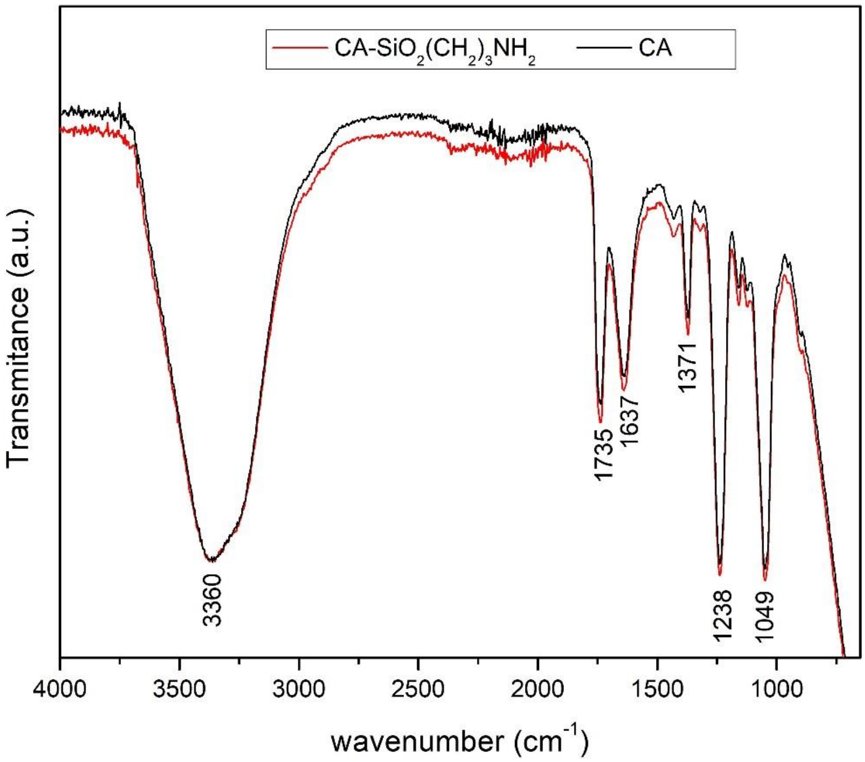

Figure 4-2. Wide-range ATR-FTIR spectra (4000-650 cm^{-1}) of the CA-SiO_2-$(CH_2)_3NH_2$ and CA membranes.

The broad band centered at ~3360 cm^{-1} is assigned to the OH stretching mode, ν(OH), and contains contributions from the hydroxyl groups of non-esterified cellulose, as well as from silanol groups and adsorbed water. Moreover, the bending fundamental, δ(OH), for the adsorbed water is located at ~1637 cm^{-1}, which has been previously described by other authors [105].

Similarly to a previous work [82], the strong carbonyl stretching mode, ν(C=O), appears at 1735 cm^{-1}, while the antisymmetric, ν_{as}(C-O-C), and symmetric, ν_s(C-O-C) stretching modes of the ester appear as strong bands at 1238 cm^{-1} and 1049 cm^{-1}, respectively.

There are no distinguishable CH stretching bands of cellulose acetate, which are possibly hindered by the broad band assigned to adsorbed water; however, in the CH deformation region, there is a medium band, typical of the methyl umbrella mode of acetate groups, at 1371 cm^{-1}.

Amine functionalization of same composition CA-SiO_2-$(CH_2)_3NH_2$ membranes has been previously proved [80], despite there being no evident band of the NH bond in Figure 4-2. In fact, primary aliphatic amines stretching mode is assigned in the region 3330-3340 cm^{-1}, for which the band, in this case, may be overlapped by the broad band which is assigned to ν(OH) [106].

Two important bands attributed to SiO_2, namely ν(Si-O-Si) and ν(Si-O-C), occur in the regions 1055 to 1165 cm^{-1} and 1115 to 1175 cm^{-1}, respectively. Similarly to previous studies [66], and due to the low silica content in the CA-SiO_2-$(CH_2)_3NH_2$ membrane, these bands are overlaid by those attributed to the ester stretching modes.

The complete assignment of the spectra of the active layer of the hybrid CA-SiO_2-$(CH_2)_3NH_2$ and pure CA membranes is presented in Table 4-1. Assignment of the ATR-FTIR spectra bands of the active layer of the hybrid and pure CA membranes.

Table 4-1. Assignment of the ATR-FTIR spectra bands of the active layer of the hybrid and pure CA membranes.

Wavenumber (cm^{-1})	Assignment
3360_{br}	ν(OH)
1735_S	ν(C=O)
1637_S	δ(OH)
1371_m	δ(CH_3)
1238_{VS}	ν_{as}(C-O-C)
1049_{VS}	ν_s(C-O-C)

br – broad; S – strong; m – medium; VS – very strong; as – asymmetric; s – symmetric.

However, this technique does not reveal a significant difference between the spectra of the two analyzed membranes. Two main factors are responsible for this: i) the very low amount of both SiO_2 and -NH_2 groups in the membrane composition and ii) the superposition of the characteristic peaks of CA, silica and amine groups. Nevertheless, the differences of permeation performance of the amine-functionalized membrane, when compared to the pure CA membrane, is an additional indicator of the presence of -NH_2 groups in the fabricated membrane.

4.2. Characterization of the SHDMM: pressure profile, pressure drop, transmembrane pressure, microchannel height, shear rate and shear stress at the wall

Figure 4-3 shows the values of ΔP and TMP obtained when DI water is circulated through the SHDMM containing the CA-SiO_2-$(CH_2)_3NH_2$ membrane at different values of Q_F. The values of ΔP were 54, 68, 83, 99, 114, 128, and 142 mmHg for Q_F values of 49, 66, 82, 99, 115, 132 and 148 mL/min, respectively. The values of TMP were 45, 53, 61, 71, 80, 90 and 100 mmHg for Q_F values of 49, 66, 82, 99, 115, 132 and 148 mL/min, respectively.

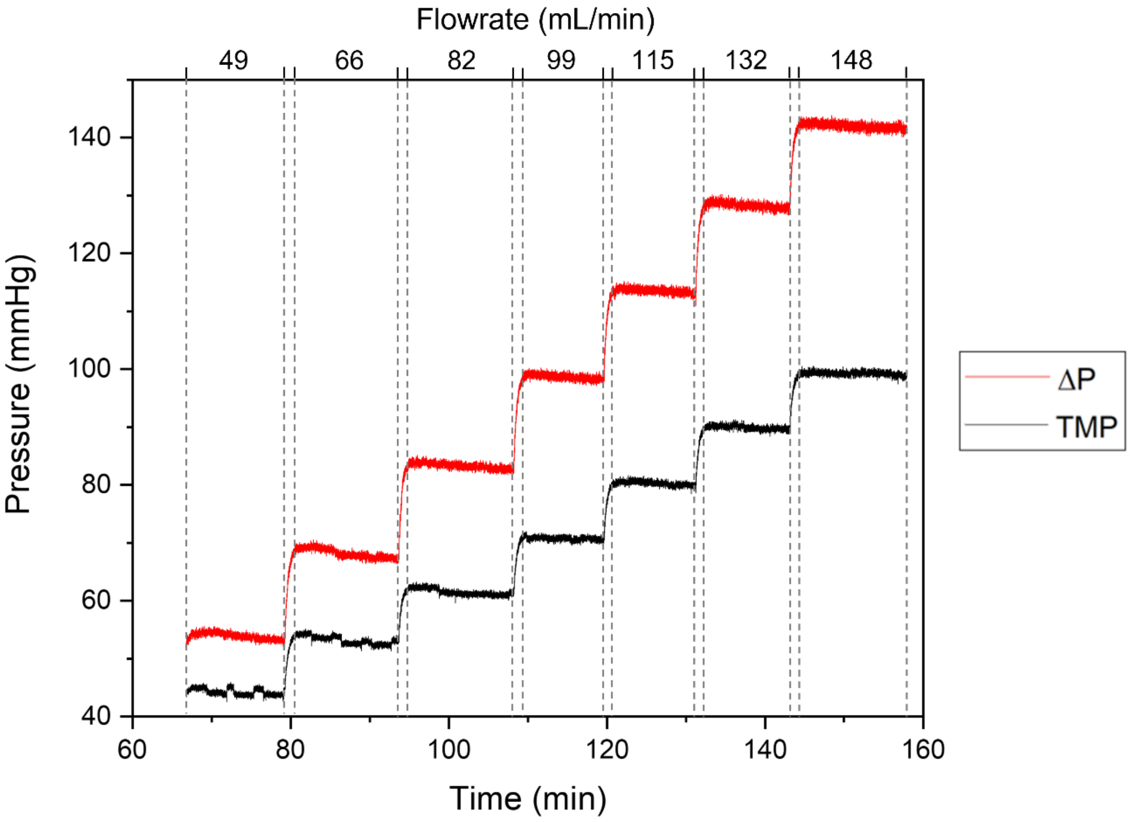

Figure 4-3. ΔP (red line) and TMP (black line) values obtained for the flow of DI water through the SHDMM circuit at different values of Q_F, which are delimited by the dashed lines.

Typical values of Q_F under which commercial hemodialysis equipment operate range from 250 to 400 mL/min [107,108] and TMP should not exceed 300 mmHg, according to the European Renal Best Practice (ERBP) [109], with the latter in the same range as the operating conditions of the SHDMM circuit. The Q_F is, however, below the typical values of hemodialysis equipment to avoid high values of sheer rate, as described below.

Considering the viscosity of water at 37ºC, μ_{water} = 0.6913 mPa.s [110], the height of the feed microchannel, calculated by Equation 3-6 was 205 ± 3 μm and 255 ± 10 μm, when the CA-SiO_2-$(CH_2)_3NH_2$ and CA membranes were placed inside the SHDMM, respectively. The difference in channel height of the SHDMM feed channel when it incases the CA membrane is expected, as the total thickness of this membrane is approximately 50 µm lower than the thickness of CA-SiO_2-$(CH_2)_3NH_2$ membrane.

The shear rate for each of the values of Q_F was calculated by Equation 2-11 and was found to be 3887, 5235, 6504, 7852, 9122, 10470 and 11739 s^{-1} for Q_F values of 49, 66, 82, 99, 115, 132 and 148 mL/min, respectively. It is known that high fluid shear triggers the activation of platelets and their subsequent aggregation [111]. An in vitro study by Holme et. al. showed that platelet activation and aggregation was observed at shear rates of 10500 s^{-1} and above [112]. Therefore, it is safe to use all of the tested feed flow rates up until 115 mL/min.

The pressure measurement in the SHDMM is of paramount importance to assess the occurrence of fouling effects, as indicated by an increase in the pressure drop across the feed flow channel with subsequent decrease of the microchannel height (Equation 3-6). However, due to limitations inherent to the experimental setup, the pressure sensors are not placed immediately at the inlet nor the at outlet of the microchannels. Instead, they are connected by a T-shaped fitting in tubes approximately 12.3 cm away from the inlet and outlet of the SHDMM. The occurrence of pressure drops in these segments was analyzed according to the Hagen-Poiseuille law [113], which describes the pressure drop in an incompressible and Newtonian fluid, in laminar flow, flowing through a cylindrical pipe of constant cross section. The Hagen-Poiseuille law is defined by

$$\Delta P = \frac{8\mu QL}{\pi R^4} \tag{4-1}$$

where ΔP is the pressure drop across L, the length of the pipe, μ is the fluid viscosity, Q is the flowrate and R is the pipe radius.

The influence of the pressure sensors position on the microchannel height was evaluated considering the pressure drop in the conditions of the hydraulic permeability experiment.

Table 4-2. Pressure drop registered throughout the hydraulic permeability experiment, corrected values taking into account the distance between the sensors and the SHDMM, and microchannel height in each scenario.

ΔP (mmHg)	2B (µm)	ΔP corrected (mmHg)	2B (µm)
54	199	54	199
68	203	68	203
83	204	83	205
99	205	98	205
114	206	113	206
128	207	128	207
142	208	141	208

The results in Table 4-2 evidence that there were no significant differences regarding the channel height, indicating that the pressure drop in the tubes has little to no influence on that of the SHDMM. In fact, the average height of the channel is (205 ± 3) μm, whether assuming the initial pressure drop or considering the corrected pressure drop values. These results hereby validate the data recorded by the pressure sensors as a realistic measurement of the SHDMM pressure drop.

4.3. Permeation experiments under dynamic conditions

4.3.1. Water permeability

In order to calculate the ultrafiltration flux, through Equation 3-11, the permeation area must be known. In this regard, three hypotheses were conjectured: O-ring, Laminar and Cell-Perforated area. The O-ring area hypothesis stated that permeation is achieved throughout the entire length of the membrane, enclosed by the O-ring, while in the Laminar area hypothesis, the feed solution would be permeated solely through the laminar region in unit III (Figure 3-2). In the Cell-Perforated area hypothesis, only the pores that constitute the grey region in unit III (Figure 3-2) would allow the fluid to be permeated. The areas relative to the O-ring, Laminar and Cell-perforated hypotheses are 105, 60 and 20.9 cm^2, respectively.

The assessment of the correct hypothesis was done by comparing the hydraulic permeability of the hybrid CA-SiO_2-$(CH_2)_3NH_2$ membrane calculated in each scenario (Figure 4-4) with the values obtained in an UF system from previous studies. For the sake of standardization, the ultrafiltration fluxes of both membranes were corrected to 25°C through Equation 3-16, allowing the comparison of performance between different systems, and L_P values are presented in commonly used units in membrane industry (kg.h^{-1}.m^{-2}.bar^{-1}).

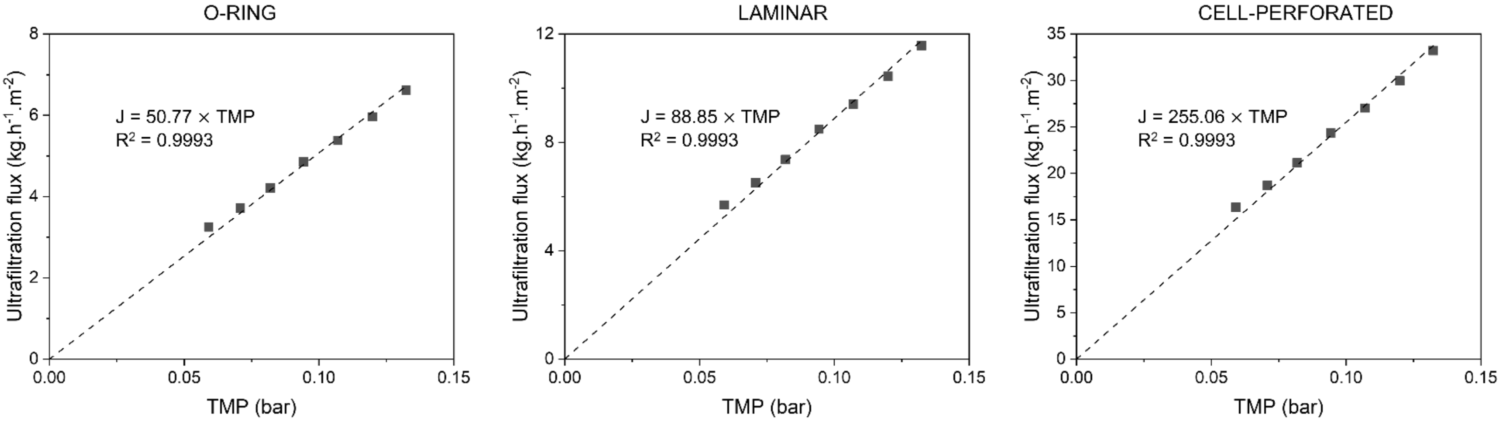

Figure 4-4. Ultrafiltration flux of pure water at 37°C as a function of the transmembrane pressure for the hybrid CA-SiO_2-$(CH_2)_3NH_2$ membrane, according to the three hypotheses. The membrane permeation area in the O-ring, Laminar and Cell-Perforated cases, was 105, 60 and 20.9 cm^2.

Previous studies on the CA-SiO_2-$(CH_2)_3NH_2$ tested in different UF systems than that of SHDMM have found an hydraulic permeability of 58.88 kg.h^{-1}.m^{-2}.bar^{-1} [114] in a cross-flow UF system, and of 27.42 kg.h^{-1}.m^{-2}.bar^{-1} in Celfa P-28 [80]. These results suggest that the effective permeation area of the membrane is that of the O-ring, i.e., 105 cm^2. Furthermore, this value indicates that permeation occurs throughout the whole length of the membrane that is in contact with the feed fluid.

Figure 4-5 shows the results of ultrafiltration flux, J, as a function of TMP obtained for the CA-SiO_2-$(CH_2)_3NH_2$ and pure CA membranes. The water permeability, L_P, of the CA-SiO_2-$(CH_2)_3NH_2$ and pure CA membranes was 89.40 mL.h^{-1}.m^{-2}.mmHg^{-1} and 49.78 mL.h^{-1}.m^{-2}.mmHg^{-1}, respectively. The introduction of silica followed by functionalization with amine groups increased the hydraulic permeability of the hybrid membrane by a factor of 1.8 when compared to the pure CA membrane. Furthermore, both membranes fall in the category of high-flux membranes since they present an L_P greater than 20 mL.h^{-1}.m^{-2}.mmHg^{-1}.

Additionally, the overall results regarding the L_P of the hybrid CA-SiO_2-$(CH_2)_3NH_2$ and pure CA membranes, considering an effective permeation area of 105 cm^2 are summarized in Table 4-3.

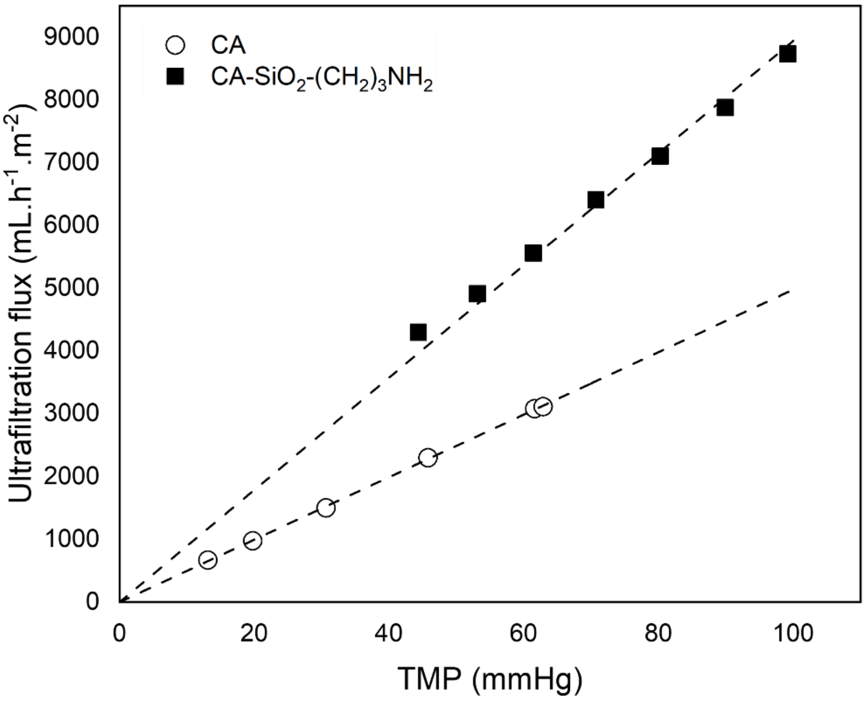

Figure 4-5. Ultrafiltration flux of pure water at 37°C as a function of the transmembrane pressure for CA-SiO_2-$(CH_2)_3NH_2$ (■) and pure CA (○) membranes. The dotted lines represent the linear fit which enables the determination of each membrane L_P.

Table 4-3. Hydraulic permeability values obtained for the hybrid CA-SiO_2-$(CH_2)_3NH_2$ and pure CA membranes, at 37ºC and 25ºC.

Membrane	**Hydraulic permeability (L_P)**	
	T = 37ºC ($mL.h^{-1}.m^{-2}.mmHg^{-1}$)	T = 25ºC ($kg.h^{-1}.m^{-2}.bar^{-1}$)
CA-SiO_2-$(CH_2)_3NH_2$	89.40	50.77
CA	49.78	28.27

Current hemodialysis equipment should deliver ultrafiltration rates between 10 to 13 mL/(h.kg) [115], under an operating TMP between 100 to 150 mmHg. Hence, for a 70 kg adult, the expected ultrafiltration rate in a clinical scenario should not be lower than 700 mL/h. Considering the estimated value of L_P for the CA-SiO_2-$(CH_2)_3NH_2$ membrane, 89.40 $mL.h^{-1}.m^{-2}.mmHg^{-1}$, and for an average TMP of 125 mmHg, in order to achieve the 700 mL/h threshold, a total membrane surface area of 0.06 m^2 is required. This is a promising result, as the estimated surface area is well below the effective permeation area of typical hemodialyzers, which ranges from 0.8 to 2.2 m^2 [8].

4.3.2. Molecular weight cut-off (MWCO)

The MWCO was determined by two methods which are shown in Figure 4-6. The upper part of the curve resembles a plateau, hindering an accurate determination of the value corresponding to the intersection of the rejection coefficient curve with the horizontal rejection line (R = 90%). Hence, to overcome this ambiguity, the higher range of rejection coefficients was linearized, namely those corresponding to PEG 35000, PEG 20000 and PEG 10000, allowing a precise determination of the intersection point.

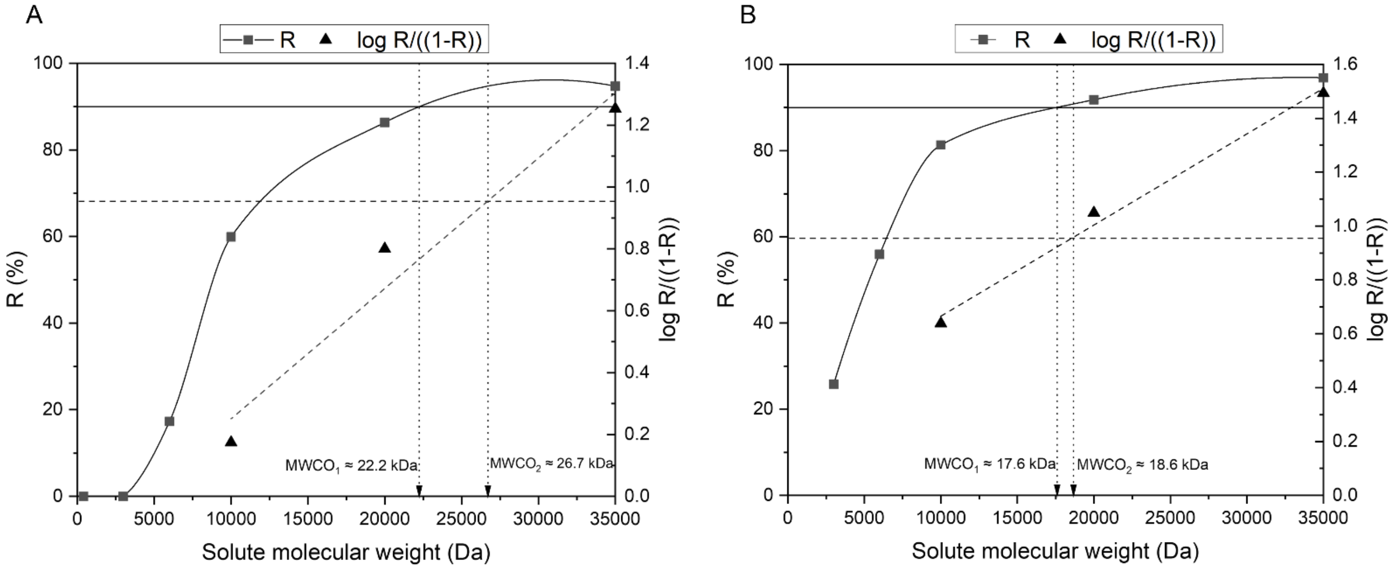

Figure 4-6. Rejection coefficient profiles of the CA-SiO_2-$(CH_2)_3NH_2$ (**A**) and CA (**B**) membranes to solutes with increasing molecular weights: 400, 3000, 6000, 10000, 20000 and 35000 Da. The horizontal full lines are set for a rejection of 90%, i.e. $\log\left(\frac{R}{1\text{-}R}\right)=0.95$. The dashed rejection lines represent the linearization of the rejection coefficients obtained for 3 different molecular weight solutes: 10000, 20000 and 35000 Da. The dotted dropdown lines indicate the estimated MWCO according to the method employed.

The depicted values of MWCO correspond to the intersection point of the plotted rejection coefficient curve ($MWCO_1$) and subsequent linearization ($MWCO_2$) with the respective horizontal rejection line. Hence, the MWCO is estimated to range between 22.2 and 26.7 kDa, for the CA-SiO_2-$(CH_2)_3NH_2$ membrane, and between 17.6 and 18.6 kDa, for the CA membrane. With the understanding that both membranes reject solutes with MWs greater than 20 kDa, it is predicted that vital blood components such as albumin, platelets and blood cells will be rejected by both membranes. Furthermore it is envisioned that molecules belonging to two different classes of uremic toxins proposed by the EUTox, small water-soluble compounds and middle molecules, can be removed as they are able to cross the membrane. Prototypes to small water-soluble compounds and middle molecules include urea, and β_2-microglobulin with a respective MW of 60 Da and 11818 Da [69]. The third group of uremic toxins, PBUTs, remain a challenge; whilst the free fraction of these molecules (MW < 500 Da) is able to cross the membrane and successfully be removed from the blood circulation, the rejection of the bound fraction will be hindered by the large MW associated to the complexes that they form with albumin (> 60 kDa).

4.3.3. Rejection coefficients to low-molecular weight water-soluble uremic toxins

Permeation experiments to prototype low-molecular weight water-soluble UTs, urea, creatinine, and uric acid, were performed considering the highest reported concentrations found in uremic populations. Feed and permeate samples were collected at times 0, 15, 30, 45, 60, 75, 90 and 105 minutes, with the respective concentration represented in Figure 4-7.

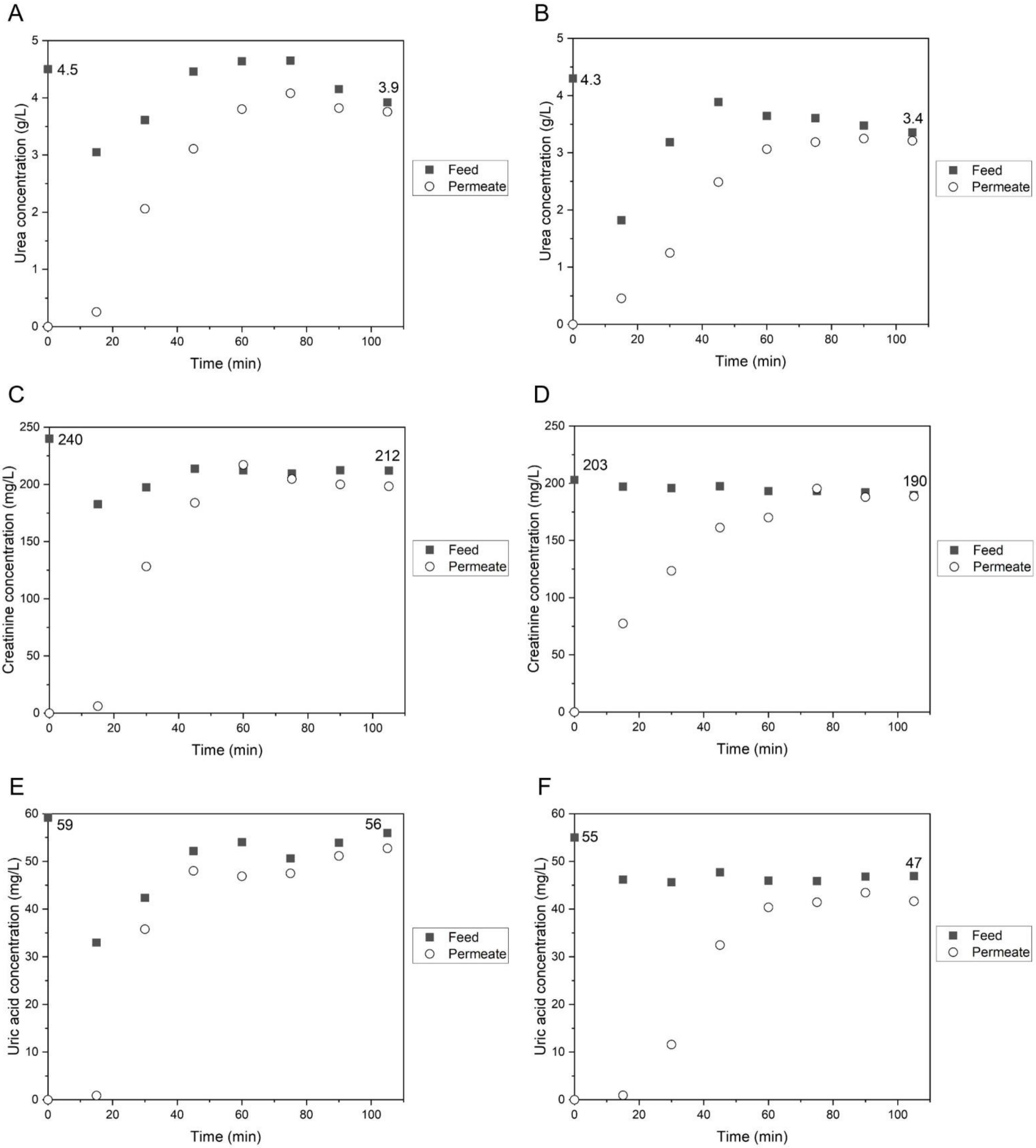

Figure 4-7. Concentration profiles of urea, creatinine, and uric acid for CA-SiO$_2$-(CH$_2$)$_3$NH$_2$ (**A**, **C** and **E**) and CA (**B**, **D** and **F**) membranes, regarding feed (■) and permeate (○) samples, for a total experiment time of 105 minutes. The initial feed concentrations aim to represent those of uremic populations.

The CA-SiO_2-$(CH_2)_3NH_2$ and CA membranes exhibit a similar behavior in terms of permeation of the three UTs studied. The initial concentrations of the feed solutions were defined according to the highest reported concentrations found in ESRD patients for the three uremic toxins [70,99] and these were measured after they had been prepared and before they were fed into the SHDMM system (t = 0 min). It is to be noted that while the highest reported uremic concentration for uric acid is 83 mg/L, the limit of solubility of this toxin in water, at 20°C, is 60 mg/L.

Prior to each experiment, the SHDMM system is primed with water so that there are no air bubbles present in the system, as well as to prevent the CA and CA-SiO_2-$(CH_2)_3NH_2$ membranes from becoming dry. The priming volume of the system is approximately 130 mL and, when the initial feed solution containing each of the three toxins is circulated into the SHDMM system, a dilution occurs. This explains the decrease of the initial concentration of the primary feed solution at t = 0 min (measured after it is prepared and before it is fed into the SHDMM system) and the moment it is collected after 15 minutes of circulation in the system (t = 15 min).

In general, for both the CA and CA-SiO_2-$(CH_2)_3NH_2$ membranes, it is observed that, between 15 and approximately 50 minutes, the concentration of the solutes in the feed compartment increases, and this can be explained by the decrease of water in the system which is constantly being removed by convection from the feed compartment through the membrane and into the permeate channel. Between 50 and 105 minutes, the concentration of the feed solution tends to stabilize at values close to the ones of the initial feed solution. To make this clear, the values of the initial and final concentrations of the feed solution are shown in each graphic of Figure 4-7.

Regarding the concentration of the permeate solution, at the beginning of the experiment (t = 0 min), the collecting permeate chamber is filled with water and as expected, the solute concentration in the permeate chamber is 0. The concentrations of the permeate solution increase considerably between 0 and approximately 50 minutes and, towards the end of the experiment (t > 80 min), they approach concentration values similar to those of the feed solution (at the corresponding time). This behavior clearly demonstrates that the membranes are permeable to the three low-molecular weight water-soluble uremic toxins evaluated: urea, creatinine, and uric acid.

The rejection coefficients (Equation 3-17) were calculated after 105 minutes of permeation. The rejection coefficient of the CA-SiO_2-$(CH_2)_3NH_2$ and CA membranes towards uric acid was 6% and 11%, respectively and towards urea, both membranes have a rejection coefficient of 4%. The rejection coefficient of the CA-SiO_2-$(CH_2)_3NH_2$ and CA membranes towards creatinine was 7% and 1%, respectively. These results are in agreement with was discussed before in terms of the MWCO, given that urea (60 Da), creatinine (113 Da) and uric acid (168 Da) have much lower MWs than the MWCO of the CA-SiO_2-$(CH_2)_3NH_2$ and CA membranes.

4.3.4. Bovine serum albumin (BSA) filtration

Figure 4-8 shows the concentration profiles of BSA in the feed and permeate channels of the SHDMM equipped with the CA-SiO_2-$(CH_2)_3NH_2$ (Figure 4-8 A) and CA (Figure 4-8 B) throughout recirculation experiments lasting 465 mins. The aim of this experiment is to determine the rejection coefficients of the CA-SiO_2-$(CH_2)_3NH_2$ and CA membranes towards BSA and assess the potential fouling of the membrane mostly attributed to irreversible protein deposition and pore blockage.

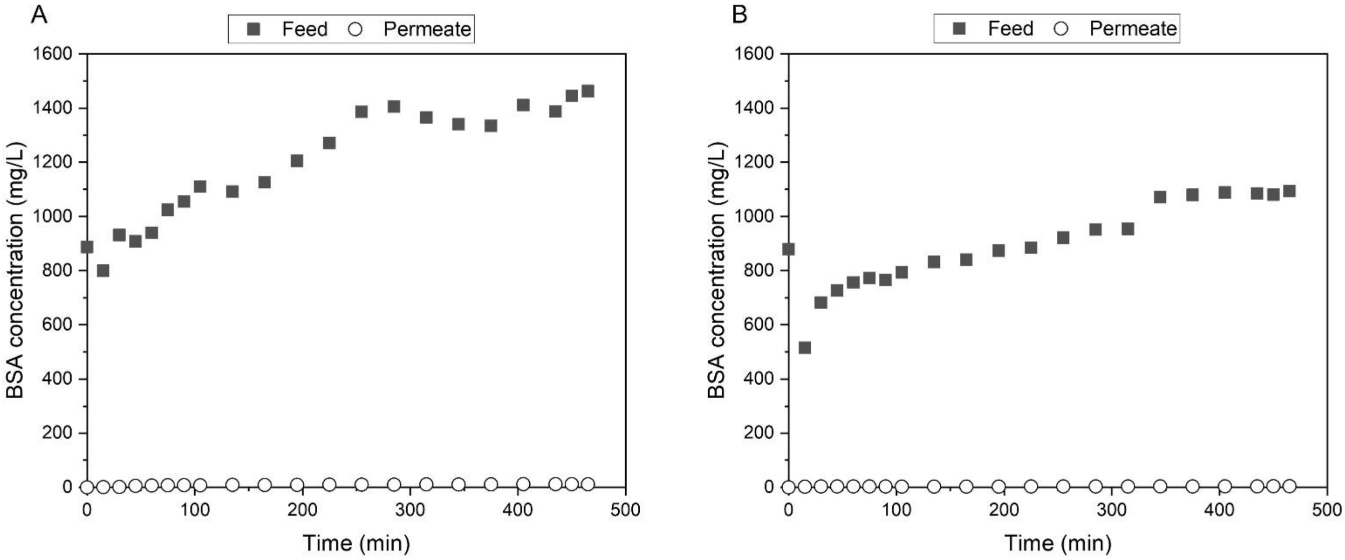

Figure 4-8. BSA concentration profiles for CA-SiO_2-$(CH_2)_3NH_2$ (A) and CA (B) membranes, regarding feed (■) and permeate (○) samples, for a total experiment time of 465 minutes.

As was described for the UT permeation experiments (Section 4.3.3), prior to initiating the filtration of the BSA solution with initial concentrations of 884 ± 4 mg/L, the SHDMM system was primed with approximately 130 mL of water. This explains the decrease in concentration of the initial feed solutions of BSA between 0 and 15 minutes. From 15 to 465 minutes, the concentration of BSA in the feed solution of both permeation experiments through the CA and CA-SiO_2-$(CH_2)_3NH_2$ membranes, increased steadily. This gives a clear indication that both membranes fully reject BSA.

At the beginning of each experiment (t = 0 min), the permeate chamber was filled with water and therefore the permeate concentration was 0 mg/L. The permeation experiments were carried out for over 7 hours and, throughout the entire experiment, the highest concentration of BSA detected in the permeate was 12 mg/L.

Furthermore, there seems to be no clear evidence of fouling events, as both the TMP and the ΔP remained approximately constant throughout the experiment, at 57 ± 7 mmHg and 87 ± 3 mmHg for the CA-SiO_2-$(CH_2)_3NH_2$ membrane, and at 47 ± 3 mmHg and 58 ± 2 mmHg for the CA membrane, respectively. The ultrafiltration rate did not change significantly in any of the two membranes throughout the long-term filtration experiment adding more evidence to support the absence of membrane fouling. The heights of the feed microchannel were calculated at the end of the experiment and were 215 μm and 246 μm, when the SHDMM encased the CA-SiO_2-$(CH_2)_3NH_2$ and CA membranes, respectively. These values are very similar to those found using pure water at Q_F of 100 mL/min (see section 3.5.3): 205 μm and 255 μm, for the SHDMM with the CA-SiO_2-$(CH_2)_3NH_2$ and CA membranes, respectively. This indicates that the protein deposition is negligible as there is no evident narrowing of the microchannel height even after 465 mins of BSA filtration.

The rejection coefficient towards BSA was calculated with the BSA concentrations measured at the end of the experiment (after 465 minutes of filtration) and was 99% for both the CA-SiO_2-$(CH_2)_3NH_2$ and CA membranes. These results were expected given that BSA has a MW of 66.5 kDa which is similar to human serum albumin [76], and the MWCO of the CA-SiO_2-$(CH_2)_3NH_2$ and CA membranes is below 27 kDa and 19 kDa, respectively. Furthermore, both membranes exhibit promising results in terms of inhibiting albumin leakage, which is highly undesirable in a clinical scenario, during HD sessions.

Conclusions

A novel integrally skinned amine-functionalized cellulose acetate-based monophasic membrane, CA-SiO_2-$(CH_2)_3NH_2$, was synthesized by an innovative method which combines the phase inversion and sol-gel techniques.

SEM micrographs of the CA-SiO_2-$(CH_2)_3NH_2$ membrane cross-sections confirmed the existence of a thin dense active layer and a much thicker, porous layer. SEM analysis revealed that the total thickness of the CA-SiO_2-$(CH_2)_3NH_2$ membrane, 103 µm, was approximately two times higher than the thickness of the CA membrane, 54 µm. ATR-FTIR analysis revealed the presence of CA based membranes.

Permeation studies showed enhanced mass transfer properties for the monophasic hybrid membrane when compared to the pure CA membrane, as evidenced by the increase of hydraulic permeability, measured at 37°C, from 49.78 $mL.h^{-1}.m^{-2}.mmHg^{-1}$, for the CA membrane, to 89.40 $mL.h^{-1}.m^{-2}.mmHg^{-1}$, for the CA-$SiO_2$-$(CH_2)_3NH_2$ membrane. Furthermore, the MWCO also increased from 18.1 kDa, for the CA membrane, to 24.5 kDa, for the CA-SiO_2-$(CH_2)_3NH_2$ membrane. Both membranes assured the permeation of water-soluble toxins such as urea, creatinine, and uric acid. Long-term continuous studies of BSA filtration revealed that both membranes completely reject albumin and there is no evidence of irreversible fouling or albumin leakage in the SHDMM.

Perspectives of future work

Further characterization studies of the monophasic hybrid CA-SiO_2-$(CH_2)_3NH_2$ membrane in terms of the chemical composition are envisioned. X-ray photoelectron spectroscopy (XPS) and nuclear magnetic resonance (NMR) spectroscopy are two techniques that are planned to prove the presence and ultimately the quantification of SiO_2 and -NH_2 at the active layer surface of the membrane.

An efficient analytical technique for the detection and quantification of free and bound forms of the toxins (PBUTs) in the feed and permeate samples should be developed and optimized. The method should be specifically directed towards quantification of the two most problematic PBUTs, indoxyl sulfate and p-cresyl sulfate, which are known for the emission of fluorescence signals.

The development of other monophasic hybrid CA-SiO_2-$(CH_2)_3NH_2$ based membranes functionalized with albumin displacers is also planned. Certain pharmacological compounds, such as ibuprofen and furosemide are known to have very high affinities with albumin and may act as competitive binders to albumin, allowing for the displacement of PBUTs.

The membrane hemocompatibility should be evaluated according to ISO 10993-4:2017 standards for the biological evaluation of medical devices, regarding the selection of tests for interactions with blood.

An additional and significant improvement in terms of the experiment set-up used for the characterization of membranes for the artificial kidney would be the development and production of a new, smaller SHDMM device which requires a smaller effective membrane surface area as well as lower priming volumes.

References

[1] R. Singh, Chapter 1 - Introduction to membrane technology, in: R. Singh (Ed.), Hybrid Membrane Systems for Water Purification, Elsevier Science, Amsterdam, 2005: pp. 1–56. https://doi.org/10.1016/B978-185617442-8/50002-6.

[2] P.M. Bungay, H.K. Lonsdale, M.N. Pinho, eds., Synthetic Membranes: Science, Engineering and Applications, Springer Netherlands, Dordrecht, 1986. https://doi.org/10.1007/978-94-009-4712-2.

[3] C.G. Gebelein, ed., Polymeric Materials and Artificial Organs, American Chemical Society, Washington, D.C., 1984. https://doi.org/10.1021/bk-1984-0256.

[4] P.S. Malchesky, K.D. Murray, D.B. Olsen, F.J. Schoen, Chapter 8 - Artificial Organs, in: B.D. Ratner, A.S. Hoffman, F.J. Schoen, J.E. Lemons (Eds.), Biomaterials Science, Academic Press, San Diego, 1996: pp. 389–412. https://doi.org/10.1016/B978-0-08-050014-0.50013-4.

[5] KidneyX Artificial Kidney Prize, KidneyX Artificial Kidney Prize. (n.d.). https://akp.kidneyx.org/ (accessed October 5, 2021).

[6] N.R. Hill, S.T. Fatoba, J.L. Oke, J.A. Hirst, C.A. O'Callaghan, D.S. Lasserson, F.D.R. Hobbs, Global Prevalence of Chronic Kidney Disease – A Systematic Review and Meta-Analysis, PLoS ONE. 11 (2016) e0158765. https://doi.org/10.1371/journal.pone.0158765.

[7] J.V. Bonventre, F.P. Hurst, M. West, I. Wu, P. Roy-Chaudhury, M. Sheldon, A Technology Roadmap for Innovative Approaches to Kidney Replacement Therapies: A Catalyst for Change, CJASN. 14 (2019) 1539–1547. https://doi.org/10.2215/CJN.02570319.

[8] C.C. Magee, J.K. Tucker, A.K. Singh, eds., Core Concepts in Dialysis and Continuous Therapies, Springer US, Boston, MA, 2016. https://doi.org/10.1007/978-1-4899-7657-4.

[9] R. Sinnakirouchenan, J.L. Holley, Peritoneal Dialysis Versus Hemodialysis: Risks, Benefits, and Access Issues, Advances in Chronic Kidney Disease. 18 (2011) 428–432. https://doi.org/10.1053/j.ackd.2011.09.001.

[10] B. Wong, P. Ravani, M.J. Oliver, J. Holroyd-Leduc, L. Venturato, A.X. Garg, R.R. Quinn, Comparison of Patient Survival Between Hemodialysis and Peritoneal Dialysis Among Patients Eligible for Both Modalities, 71 (2018) 8.

[11] K.V. Peinemann, S.P. Nunes, eds., Membranes for life sciences, Wiley-VCH, Weinheim, 2008.

[12] M. Mulder, Basic Principles of Membrane Technology, Springer Netherlands, Dordrecht, 1991. https://doi.org/10.1007/978-94-017-0835-7.

[13] W.S.W. Ho, K.K. Sirkar, eds., Membrane Handbook, Springer US, Boston, MA, 1992. https://doi.org/10.1007/978-1-4615-3548-5.

[14] K. Scott, Handbook of industrial membranes, 1st ed, Elsevier Advanced Technology, Oxford, 1995.

[15] N. Abdullah, M.A. Rahman, M.H. Dzarfan Othman, J. Jaafar, A.F. Ismail, Chapter 2 - Membranes and Membrane Processes: Fundamentals, in: A. Basile, S. Mozia, R. Molinari (Eds.), Current Trends and Future Developments on (Bio-) Membranes, Elsevier, 2018: pp. 45–70. https://doi.org/10.1016/B978-0-12-813549-5.00002-5.

[16] A. Lee, J.W. Elam, S.B. Darling, Membrane materials for water purification: design, development, and application, Environ. Sci.: Water Res. Technol. 2 (2016) 17–42. https://doi.org/10.1039/C5EW00159E.

[17] H.P. Hsieh, Inorganic Membrane Reactors, Null. 33 (1991) 1–70. https://doi.org/10.1080/01614949108020296.

[18] M.A.A. El-Ghaffar, H.A. Tieama, A Review of Membranes Classifications, Configurations, Surface Modifications, Characteristics and Its Applications in Water Purification, (n.d.) 26.

[19] G.Q. Lu, J.C. Diniz da Costa, M. Duke, S. Giessler, R. Socolow, R.H. Williams, T. Kreutz, Inorganic membranes for hydrogen production and purification: A critical review and perspective, Journal of Colloid and Interface Science. 314 (2007) 589–603. https://doi.org/10.1016/j.jcis.2007.05.067.

[20] J.M. Gohil, R.R. Choudhury, Introduction to Nanostructured and Nano-enhanced Polymeric Membranes: Preparation, Function, and Application for Water Purification, in: Nanoscale Materials in Water Purification, Elsevier, 2019: pp. 25–57. https://doi.org/10.1016/B978-0-12-813926-4.00038-0.

[21] M.N. de Pinho, M. Minhalma, Introduction in Membrane Technologies, in: Separation of Functional Molecules in Food by Membrane Technology, Elsevier, 2019: pp. 1–29. https://doi.org/10.1016/B978-0-12-815056-6.00001-2.

[22] K. Khulbe, C. Feng, T. Matsuura, Synthetic Polymeric Membranes: Characterization by Atomic Force Microscopy, 2008. https://doi.org/10.1007/978-3-540-73994-4.

[23] H. Strathmann, L. Giorno, E. Drioli, Basic Aspects in Polymeric Membrane Preparation, in: Comprehensive Membrane Science and Engineering, 2010: pp. 91–112. https://doi.org/10.1016/B978-0-08-093250-7.00057-8.
[24] R.W. Baker, Membrane technology and applications, McGraw-Hill, New York, 2000.
[25] S.M. Jamil, M.H.D. Othman, M.A. Rahman, J. Jaafar, A.F. Ismail, K. Li, Recent fabrication techniques for micro-tubular solid oxide fuel cell support: A review, Journal of the European Ceramic Society. 35 (2015) 1–22. https://doi.org/10.1016/j.jeurceramsoc.2014.08.034.
[26] H. Strathmann, K. Kock, P. Amar, R.W. Baker, The formation mechanism of asymmetric membranes, Desalination. 16 (1975) 179–203. https://doi.org/10.1016/S0011-9164(00)82092-5.
[27] R.E. Kesting, A. Menefee, The role of formamide in the preparation of cellulose acetate membranes by the phase inversion process, Kolloid-Z.u.Z.Polymere. 230 (1969) 341–346. https://doi.org/10.1007/BF01520608.
[28] K. Sumida, K. Liang, J. Reboul, I.A. Ibarra, S. Furukawa, P. Falcaro, Sol–Gel Processing of Metal–Organic Frameworks, Chem. Mater. 29 (2017) 2626–2645. https://doi.org/10.1021/acs.chemmater.6b03934.
[29] S. Rahim, F. Jan Iftikhar, M.I. Malik, Chapter 16 - Biomedical applications of magnetic nanoparticles, in: M.R. Shah, M. Imran, S. Ullah (Eds.), Metal Nanoparticles for Drug Delivery and Diagnostic Applications, Elsevier, 2020: pp. 301–328. https://doi.org/10.1016/B978-0-12-816960-5.00016-1.
[30] N. Varghese, T. Francis, M. Shelly, A.B. Nair, Chapter 14 - Nanocomposites of polymer matrices: Nanoscale processing, in: S. Thomas, P. Balakrishnan (Eds.), Nanoscale Processing, Elsevier, 2021: pp. 383–406. https://doi.org/10.1016/B978-0-12-820569-3.00014-1.
[31] R. Ciriminna, A. Fidalgo, V. Pandarus, F. Béland, L.M. Ilharco, M. Pagliaro, The Sol–Gel Route to Advanced Silica-Based Materials and Recent Applications, Chem. Rev. 113 (2013) 6592–6620. https://doi.org/10.1021/cr300399c.
[32] U. Schubert, N. Huesing, A. Lorenz, Hybrid Inorganic-Organic Materials by Sol-Gel Processing of Organofunctional Metal Alkoxides, Chem. Mater. 7 (1995) 2010–2027. https://doi.org/10.1021/cm00059a007.
[33] H.E. Bergna, The Colloid Chemistry of Silica, in: The Colloid Chemistry of Silica, American Chemical Society, 1994: pp. 1–47. https://doi.org/10.1021/ba-1994-0234.ch001.
[34] V. Souza, M. Quadri, Organic-inorganic hybrid membranes in separation processes: A 10-year review, Brazilian Journal of Chemical Engineering. 30 (2013) 683–700. https://doi.org/10.1590/S0104-66322013000400001.
[35] H. Cong, M. Radosz, B.F. Towler, Y. Shen, Polymer-inorganic nanocomposite membranes for gas separation, Separation and Purification Technology. 55 (2007) 281–291.
[36] G.J. Owens, R.K. Singh, F. Foroutan, M. Alqaysi, C.-M. Han, C. Mahapatra, H.-W. Kim, J.C. Knowles, Sol–gel based materials for biomedical applications, Progress in Materials Science. 77 (2016) 1–79. https://doi.org/10.1016/j.pmatsci.2015.12.001.
[37] M.A. Aegerter, M. Mennig, eds., Sol-Gel Technologies for Glass Producers and Users, Springer US, Boston, MA, 2004. https://doi.org/10.1007/978-0-387-88953-5.
[38] B. Van der Bruggen, Membrane Technology, in: John Wiley & Sons Inc (Ed.), Kirk-Othmer Encyclopedia of Chemical Technology, John Wiley & Sons, Inc., Hoboken, NJ, USA, 2017: pp. 1–47. https://doi.org/10.1002/0471238961.1305130202011105.a01.pub3.
[39] P. Pal, Chapter 1 - Introduction to the Arsenic Contamination Problem, in: P. Pal (Ed.), Groundwater Arsenic Remediation, Butterworth-Heinemann, 2015: pp. 1–23. https://doi.org/10.1016/B978-0-12-801281-9.00001-1.
[40] L.K. Wang, J.P. Chen, Y.-T. Hung, N.K. Shammas, eds., Membrane and Desalination Technologies, Humana Press, Totowa, NJ, 2011. https://doi.org/10.1007/978-1-59745-278-6.
[41] A. Cassano, C. Conidi, R. Castro-Muñoz, Current and Future Applications of Nanofiltration in Food Processing, in: Separation of Functional Molecules in Food by Membrane Technology, Elsevier, 2019: pp. 305–348. https://doi.org/10.1016/B978-0-12-815056-6.00009-7.
[42] J.D. Andrade, V. Hlady, Protein adsorption and materials biocompatibility: A tutorial review and suggested hypotheses, in: Biopolymers/Non-Exclusion HPLC, Springer Berlin Heidelberg, Berlin, Heidelberg, 1986: pp. 1–63.
[43] P.M. Doran, Unit Operations, in: Bioprocess Engineering Principles, Elsevier, 2013: pp. 445–595. https://doi.org/10.1016/B978-0-12-220851-5.00011-3.
[44] J. Ren, H.-L. Wei, L. Xu, L.-Y. Jia, 5.55 - Blood Detoxication, in: M. Moo-Young (Ed.), Comprehensive Biotechnology (Second Edition), Academic Press, Burlington, 2011: pp. 729–739. https://doi.org/10.1016/B978-0-08-088504-9.00515-8.

[45] C. Hsu, CHAPTER 2 - Clinical Evaluation of Kidney Function, in: A. Greenberg, A.K. Cheung, T.M. Coffman, R.J. Falk, J.C. Jennette (Eds.), Primer on Kidney Diseases (Fifth Edition), W.B. Saunders, Philadelphia, 2009: pp. 19–23. https://doi.org/10.1016/B978-1-4160-5185-5.00002-X.

[46] P. Delanaye, E. Schaeffner, N. Ebert, E. Cavalier, C. Mariat, J.-M. Krzesinski, O. Moranne, Normal reference values for glomerular filtration rate: what do we really know?, Nephrology Dialysis Transplantation. 27 (2012) 2664–2672. https://doi.org/10.1093/ndt/gfs265.

[47] I. Teitelbaum, J. Burkart, Peritoneal dialysis., Am J Kidney Dis. 42 (2003) 1082–1096. https://doi.org/10.1016/j.ajkd.2003.08.036.

[48] A.R. Nissenson, R.N. Fine, eds., Handbook of dialysis therapy, 5th edition, Elsevier, Philadelphia, PA, 2017.

[49] National Institute of Diabetes and Digestive and Kindey Diseases, Hemodialysis, (2018). https://www.niddk.nih.gov/health-information/kidney-disease/kidney-failure/hemodialysis (accessed October 16, 2021).

[50] O.E.M. ter Beek, D. Pavlenko, D. Stamatialis, Hollow fiber membranes for long-term hemodialysis based on polyethersulfone-SlipSkin™ polymer blends, Journal of Membrane Science. 604 (2020) 118068. https://doi.org/10.1016/j.memsci.2020.118068.

[51] D. Santoro, F. Benedetto, P. Mondello, F. Spinelli, C. Ricciardi, V. Cernaro, M. Buemi, N. Pipito', D. Barilla', Vascular access for hemodialysis: current perspectives, IJNRD. (2014) 281. https://doi.org/10.2147/IJNRD.S46643.

[52] National Institute of Diabetes and Digestive and Kidney Diseases, Hemodialysis circuit, (2019). https://www.niddk.nih.gov/news/media-library/8459 (accessed October 16, 2021).

[53] J. Vienken, Membranes in Hemodialysis, in: Membranes for the Life Sciences, John Wiley & Sons, Ltd, 2007: pp. 1–48. https://doi.org/10.1002/9783527631360.ch1.

[54] W.R. Clark, R.J. Hamburger, M.J. Lysaght, Effect of membrane composition and structure on solute removal and biocompatibility in hemodialysis, Kidney International. 56 (1999) 2005–2015. https://doi.org/10.1046/j.1523-1755.1999.00784.x.

[55] K.D. Vos, A.P. Hatcher, U. Merten, Lifetime of Cellulose Acetate Reverse Osmosis Membranes, I&EC Product Research and Development. 5 (1966) 211–218. https://doi.org/10.1021/i360019a002.

[56] B.J. Lipps, R.D. Stewart, H.A. Perkins, G.W. Holmes, E.A. McLain, M.R. Rolfs, P.D. Oja, The Hollow Fiber Artificial Kidney, Transactions - American Society for Artificial Organs. 13 (1967) 200–207.

[57] M.J. Lysaght, Hemodialysis Membranes in Transition, in: G. D'Amico, G. Colasanti (Eds.), Contributions to Nephrology, S. Karger AG, 1988: pp. 1–17. https://doi.org/10.1159/000415230.

[58] R.A. Ward, E. Klein, G.B. Harding, K.E. Murchison, Response of complement and neutrophils to hydrophilized synthetic membranes., ASAIO Trans. 34 (1988) 334–337.

[59] L.A. Pedrini, C. Krisp, A. Gmerek, D.A. Wolters, Patterns of Proteins Removed with High-Flux Membranes on High-Volume Hemodiafiltration Detected with a MultiDimensional LC-MS/MS Strategy, Blood Purif. 38 (2014) 115–126. https://doi.org/10.1159/000365745.

[60] E.M. Weissinger, T. Kaiser, N. Meert, R. De Smet, M. Walden, H. Mischak, R.C. Vanholder, for the European Uremic Toxin Work Group, Proteomics: a novel tool to unravel the patho-physiology of uraemia, Nephrology Dialysis Transplantation. 19 (2004) 3068–3077. https://doi.org/10.1093/ndt/gfh509.

[61] M.M. Speeckaert, G.L. Glorieux, R. Vanholder, W. Van Biesen, Y.E. Taes, F. Clement, C. Wehlou, J.R. Delanghe, Vitamin D Binding Protein and the Need for Vitamin D in Hemodialysis Patients, Journal of Renal Nutrition. 18 (2008) 400–407. https://doi.org/10.1053/j.jrn.2008.04.013.

[62] R. Elsen, L.K. Silva, Advantages of meltspun membrane technology compared to solution spinning., Contrib Nephrol. 103 (1993) 125–138. https://doi.org/10.1159/000422281.

[63] K.J. Edgar, C.M. Buchanan, J.S. Debenham, P.A. Rundquist, B.D. Seiler, M.C. Shelton, D. Tindall, Advances in cellulose ester performance and application, Progress in Polymer Science. 26 (2001) 1605–1688. https://doi.org/10.1016/S0079-6700(01)00027-2.

[64] K. Gastaldello, C. Melot, R.-J. Kahn, J.-L. Vanherweghem, J.-L. Vincent, C. Tielemans, Comparison of cellulose diacetate and polysulfone membranes in the outcome of acute renal failure. A prospective randomized study, Nephrology Dialysis Transplantation. 15 (2000) 224–230. https://doi.org/10.1093/ndt/15.2.224.

[65] M. Faria, C. Moreira, T. Eusébio, P. Brogueira, M.N. de Pinho, Hybrid flat sheet cellulose acetate/silicon dioxide ultrafiltration membranes for uremic blood purification, Cellulose. 27 (2020) 3847–3869. https://doi.org/10.1007/s10570-020-02985-2.

[66] G. Mendes, M. Faria, A. Carvalho, M.C. Gonçalves, M.N. de Pinho, Structure of water in hybrid cellulose acetate-silica ultrafiltration membranes and permeation properties, Carbohydrate Polymers. 189 (2018) 342–351. https://doi.org/10.1016/j.carbpol.2018.02.030.

[67] R. Vanholder, S. Van Laecke, G. Glorieux, What is new in uremic toxicity?, Pediatric Nephrology. 23 (2008) 1211–1221. https://doi.org/10.1007/s00467-008-0762-9.

[68] T. Toyohara, Y. Akiyama, T. Suzuki, Y. Takeuchi, E. Mishima, M. Tanemoto, A. Momose, N. Toki, H. Sato, M. Nakayama, A. Hozawa, I. Tsuji, S. Ito, T. Soga, T. Abe, Metabolomic profiling of uremic solutes in CKD patients, Hypertension Research. 33 (2010) 944–952. https://doi.org/10.1038/hr.2010.113.

[69] M. Faria, M.N. de Pinho, Challenges of reducing protein-bound uremic toxin levels in chronic kidney disease and end stage renal disease, Translational Research. 229 (2021) 115–134. https://doi.org/10.1016/j.trsl.2020.09.001.

[70] R. Vanholder, R. De Smet, G. Glorieux, A. Argilés, U. Baurmeister, P. Brunet, W. Clark, G. Cohen, P.P. De Deyn, R. Deppisch, B. Descamps-Latscha, T. Henle, A. Jörres, H.D. Lemke, Z.A. Massy, J. Passlick-Deetjen, M. Rodriguez, B. Stegmayr, P. Stenvinkel, C. Tetta, C. Wanner, W. Zidek, For the European Uremic Toxin Work Group (EUTox), Review on uremic toxins: Classification, concentration, and interindividual variability, Kidney International. 63 (2003) 1934–1943. https://doi.org/10.1046/j.1523-1755.2003.00924.x.

[71] F. Locatelli, F. Mastrangelo, B. Redaelli, C. Ronco, D. Marcelli, G. La Greca, G. Orlandini, Effects of different membranes and dialysis technologies on patient treatment tolerance and nutritional parameters. The Italian Cooperative Dialysis Study Group., Kidney Int. 50 (1996) 1293–1302. https://doi.org/10.1038/ki.1996.441.

[72] S. Palmer, K. Rabindranath, J. Craig, P. Roderick, F. Locatelli, G. Strippoli, High-flux versus low-flux membranes for end-stage kidney disease, Cochrane Database of Systematic Reviews. (2012). https://doi.org/10.1002/14651858.CD005016.pub2.

[73] L. Viaene, P. Annaert, H. de Loor, R. Poesen, P. Evenepoel, B. Meijers, Albumin is the main plasma binding protein for indoxyl sulfate and p-cresyl sulfate, Biopharmaceutics & Drug Disposition. 34 (2013) 165–175. https://doi.org/10.1002/bdd.1834.

[74] B.K.I. Meijers, B. Bammens, K. Verbeke, P. Evenepoel, A review of albumin binding in CKD., Am J Kidney Dis. 51 (2008) 839–850. https://doi.org/10.1053/j.ajkd.2007.12.035.

[75] S. Lekawanvijit, A.R. Kompa, H. Krum, Protein-bound uremic toxins: a long overlooked culprit in cardiorenal syndrome, American Journal of Physiology-Renal Physiology. 311 (2016) F52–F62. https://doi.org/10.1152/ajprenal.00348.2015.

[76] D.A. Belinskaia, P.A. Voronina, A.A. Batalova, N.V. Goncharov, Serum Albumin, Encyclopedia. 1 (2020) 65–75. https://doi.org/10.3390/encyclopedia1010009.

[77] G. Liu, C. Wu, X. Zhang, Y. Liu, H. Meng, J. Xu, Y. Han, X. Xu, Y. Xu, Surface functionalization of zirconium dioxide nano-adsorbents with 3-aminopropyl triethoxysilane and promoted adsorption activity for bovine serum albumin, Materials Chemistry and Physics. 176 (2016) 129–135. https://doi.org/10.1016/j.matchemphys.2016.03.042.

[78] R. Lu, W.-W. Li, A. Katzir, Y. Raichlin, H.-Q. Yu, B. Mizaikoff, Probing the secondary structure of bovine serum albumin during heat-induced denaturation using mid-infrared fiberoptic sensors, Analyst. 140 (2015) 765–770. https://doi.org/10.1039/C4AN01495B.

[79] V. Maheshwari, X. Tao, S. Thijssen, P. Kotanko, Removal of Protein-Bound Uremic Toxins Using Binding Competitors in Hemodialysis: A Narrative Review, Toxins. 13 (2021). https://doi.org/10.3390/toxins13090622.

[80] M.C. Andrade, J.C. Pereira, N. de Almeida, P. Marques, M. Faria, M.C. Gonçalves, Improving hydraulic permeability, mechanical properties, and chemical functionality of cellulose acetate-based membranes by co-polymerization with tetraethyl orthosilicate and 3-(aminopropyl)triethoxysilane, Carbohydrate Polymers. 261 (2021) 117813. https://doi.org/10.1016/j.carbpol.2021.117813.

[81] S. Loeb, S. Sourirajan, Sea Water Demineralization by Means of an Osmotic Membrane, in: Saline Water Conversion—II, American Chemical Society, 1963: pp. 117–132. https://doi.org/10.1021/ba-1963-0038.ch009.

[82] A.S. Figueiredo, A.R. Garcia, M. Minhalma, L. Ilharco, M. de Pinho, The Ultrafiltration Performance of Cellulose Acetate Asymmetric Membranes: A New Perspective on the Correlation with the Infrared Spectra, Journal of Membrane Science and Research. 6 (2020) 70–80. https://doi.org/10.22079/jmsr.2019.110424.1269.

[83] R.E. Kesting, Semipermeable membranes of cellulose acetate for desalination in the process of reverse osmosis. I. Lyotropic swelling of secondary cellulose acetate, J. Appl. Polym. Sci. 9 (1965) 663–688. https://doi.org/10.1002/app.1965.070090226.

[84] J. Brinker, G. Scherer, The Physics and Chemistry of Sol-Gel Processing, Gulf Professional Publishing, 1990.

[85] E. Staude, J. Passlack, Characterization of ultrafiltration membranes by drying, Journal of Membrane Science. 28 (1986) 209–223. https://doi.org/10.1016/S0376-7388(00)82211-5.

[86] Z.A. Jawad, A.L. Ahmad, S.C. Low, T.L. Chew, S.H.S. Zein, Influence of solvent exchange time on mixed matrix membrane separation performance for CO2/N2 and a kinetic sorption study, Journal of Membrane Science. 476 (2015) 590–601. https://doi.org/10.1016/j.memsci.2014.11.008.

[87] A. Lui, F.D.F. Talbot, T. Matsuura, S. Sourirajan, Studies on the solvent exchange technique for making dry cellulose acetate membranes for the separation of gaseous mixtures, Journal of Applied Polymer Science. 36 (1988) 1809–1820. https://doi.org/10.1002/app.1988.070360808.

[88] R.B. Bird, W.E. Stewart, E.N. Lightfoot, Transport Phenomena, 2nd ed., John Wiley&Sons Inc., 2002.

[89] M. Faria, Y. Liu, E.F. Leonard, Particle Spallation in a Microfluidic Blood Processing Device: The Problem of Using Peristaltic Pumps and Silicon-based Microfilters, Int J Artif Organs. 40 (2017) 589–593. https://doi.org/10.5301/ijao.5000609.

[90] Y. Liu, M. Faria, E. Leonard, Spallation of Small Particles From Peristaltic Pump Tube Segments: Thoughts and Progress, Artificial Organs. 41 (2017) 672–677. https://doi.org/10.1111/aor.12815.

[91] D.K. Hothi, D.F. Geary, Chapter 57 - Pediatric Hemodialysis Prescription, Efficacy, and Outcome, in: D.F. Geary, F. Schaefer (Eds.), Comprehensive Pediatric Nephrology, Mosby, Philadelphia, 2008: pp. 867–893. https://doi.org/10.1016/B978-0-323-04883-5.50063-5.

[92] C. Jacobs, ed., Replacement of renal function by dialysis, 4th ed, Kluwer Academic, Dordrecht ; Boston, 1996.

[93] Biomedical Membranes and (Bio)Artificial Organs, WORLD SCIENTIFIC, 2017. https://doi.org/10.1142/10549.

[94] M. Abe, I. Masakane, A. Wada, S. Nakai, K. Nitta, H. Nakamoto, Dialyzer Classification and Mortality in Hemodialysis Patients: A 3-Year Nationwide Cohort Study, Frontiers in Medicine. 8 (2021) 1468. https://doi.org/10.3389/fmed.2021.740461.

[95] M.J. Rosa, Separação Seletiva de Compostos Orgânicos de Correntes Aquosas por Ultrafiltração e Nanofiltração, (1995).

[96] R.W. Gallant, J.M. Railey, Physical Properties of Hydrocarbons, 2nd ed., Gulf Publishing Company, 1970.

[97] M. Park, S.A. Snyder, Chapter 6 - Attenuation of contaminants of emerging concerns by nanofiltration membrane: rejection mechanism and application in water reuse, in: A.J. Hernández-Maldonado, L. Blaney (Eds.), Contaminants of Emerging Concern in Water and Wastewater, Butterworth-Heinemann, 2020: pp. 177–206. https://doi.org/10.1016/B978-0-12-813561-7.00006-7.

[98] E.S. Perry, C.J. van Oss, Progress in separation and purification, Wiley-Interscience, New York, 1970.

[99] F. Duranton, G. Cohen, R. De Smet, M. Rodriguez, J. Jankowski, R. Vanholder, A. Argiles, on behalf of the European Uremic Toxin Work Group, Normal and Pathologic Concentrations of Uremic Toxins, JASN. 23 (2012) 1258–1270. https://doi.org/10.1681/ASN.2011121175.

[100] Z. Filutowicz, K. Łukaszewski, K. Pieszyński, Remarks on spectra-photometric monitoring of urea in dialysate, Journal of Medical Informatics & Technologies. Vol. 8 (2004) MM105-110.

[101] O.E.M. ter Beek, M.K. van Gelder, C. Lokhorst, D.H.M. Hazenbrink, B.H. Lentferink, K.G.F. Gerritsen, D. Stamatialis, In vitro study of dual layer mixed matrix hollow fiber membranes for outside-in filtration of human blood plasma, Acta Biomaterialia. 123 (2021) 244–253. https://doi.org/10.1016/j.actbio.2020.12.063.

[102] H. Montaseri, H. Khajehsharifi, S. Yousefinejad, UV determination of Epinephrine, Uric Acid and Acetaminophen in pharmaceutical formulation and some of human body fluids using multivariate calibration, Química Nova. 37 (2014) 1404–1409. https://doi.org/10.5935/0100-4042.20140206.

[103] M.M. Bradford, A rapid and sensitive method for the quantitation of microgram quantities of protein utilizing the principle of protein-dye binding., Anal Biochem. 72 (1976) 248–254. https://doi.org/10.1006/abio.1976.9999.

[104] T. Zor, Z. Selinger, Linearization of the Bradford Protein Assay Increases Its Sensitivity: Theoretical and Experimental Studies, Analytical Biochemistry. 236 (1996) 302–308. https://doi.org/10.1006/abio.1996.0171.

[105] D. Murphy, M.N. de Pinho, An ATR-FTIR study of water in cellulose acetate membranes prepared by phase inversion, Journal of Membrane Science. 106 (1995) 245–257. https://doi.org/10.1016/0376-7388(95)00089-U.

[106] R.A. Nyquist, ed., Chapter 8 - Aliphatic Amines, in: Interpreting Infrared, Raman, and Nuclear Magnetic Resonance Spectra, Academic Press, San Diego, 2001: pp. 143–148. https://doi.org/10.1016/B978-012523475-7/50172-8.

[107] M. Albalate, R. Pérez-García, P. de Sequera, E. Corchete, R. Alcazar, M. Ortega, M. Puerta, Is it useful to increase dialysate flow rate to improve the delivered Kt?, BMC Nephrol. 16 (2015) 20. https://doi.org/10.1186/s12882-015-0013-9.

[108] K.Y. Chang, S.-H. Kim, Y.O. Kim, D.C. Jin, H.C. Song, E.J. Choi, Y.-L. Kim, Y.-S. Kim, S.-W. Kang, N.-H. Kim, C.W. Yang, Y.K. Kim, The impact of blood flow rate during hemodialysis on all-cause mortality, Korean J Intern Med. 31 (2016) 1131–1139. https://doi.org/10.3904/kjim.2015.111.

[109] J. Tattersall, A. Martin-Malo, L. Pedrini, A. Basci, B. Canaud, D. Fouque, P. Haage, K. Konner, J. Kooman, F. Pizzarelli, J. Tordoir, M. Vennegoor, C. Wanner, P. ter Wee, R. Vanholder, EBPG guideline on dialysis strategies, Nephrology Dialysis Transplantation. 22 (2007) ii5–ii21. https://doi.org/10.1093/ndt/gfm022.

[110] W.M. Haynes, CRC Handbook of Chemistry and Physics, 97th ed., CRC Press, 2017.

[111] M. Kroll, J. Hellums, L. McIntire, A. Schafer, J. Moake, Platelets and shear stress, Blood. 88 (1996) 1525–1541. https://doi.org/10.1182/blood.V88.5.1525.1525.

[112] P.A. Holme, U. Ørvim, M.J.A.G. Hamers, N.O. Solum, F.R. Brosstad, R.M. Barstad, K.S. Sakariassen, Shear-Induced Platelet Activation and Platelet Microparticle Formation at Blood Flow Conditions as in Arteries With a Severe Stenosis, ATVB. 17 (1997) 646–653. https://doi.org/10.1161/01.ATV.17.4.646.

[113] J.X.J. Zhang, K. Hoshino, Chapter 3 - Microfluidics and Micro Total Analytical Systems, in: J.X.J. Zhang, K. Hoshino (Eds.), Molecular Sensors and Nanodevices, William Andrew Publishing, Oxford, 2014: pp. 103–168. https://doi.org/10.1016/B978-1-4557-7631-3.00003-X.

[114] M. Lopes, Synthesis and Characterization of Novel Monophasic Hybrid Membranes of Cellulose Acetate by Co-polymerization with Tetraethyl Orthosilicate and 3-(Aminopropyl)triethoxysilane, Instituto Superior Técnico, 2021.

[115] J.E. Flythe, S.E. Kimmel, S.M. Brunelli, Rapid fluid removal during dialysis is associated with cardiovascular morbidity and mortality, Kidney International. 79 (2011) 250–257. https://doi.org/10.1038/ki.2010.383.

Appendix A. Pump calibration

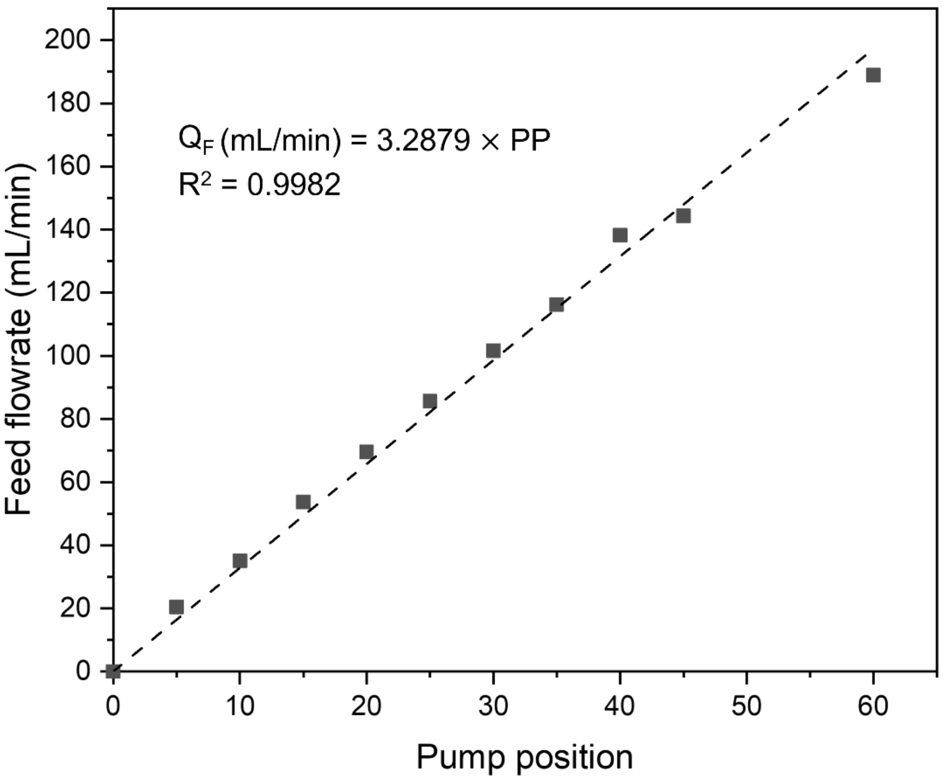

Figure A-1. Pump calibration curve of the ECOLINE VC-360 pump, illustrating the feed flowrate as a function of the pump position. The equation is the result of a linear fit, with the respective coefficient of correlation (R^2).

Appendix B. TOC calibration curves

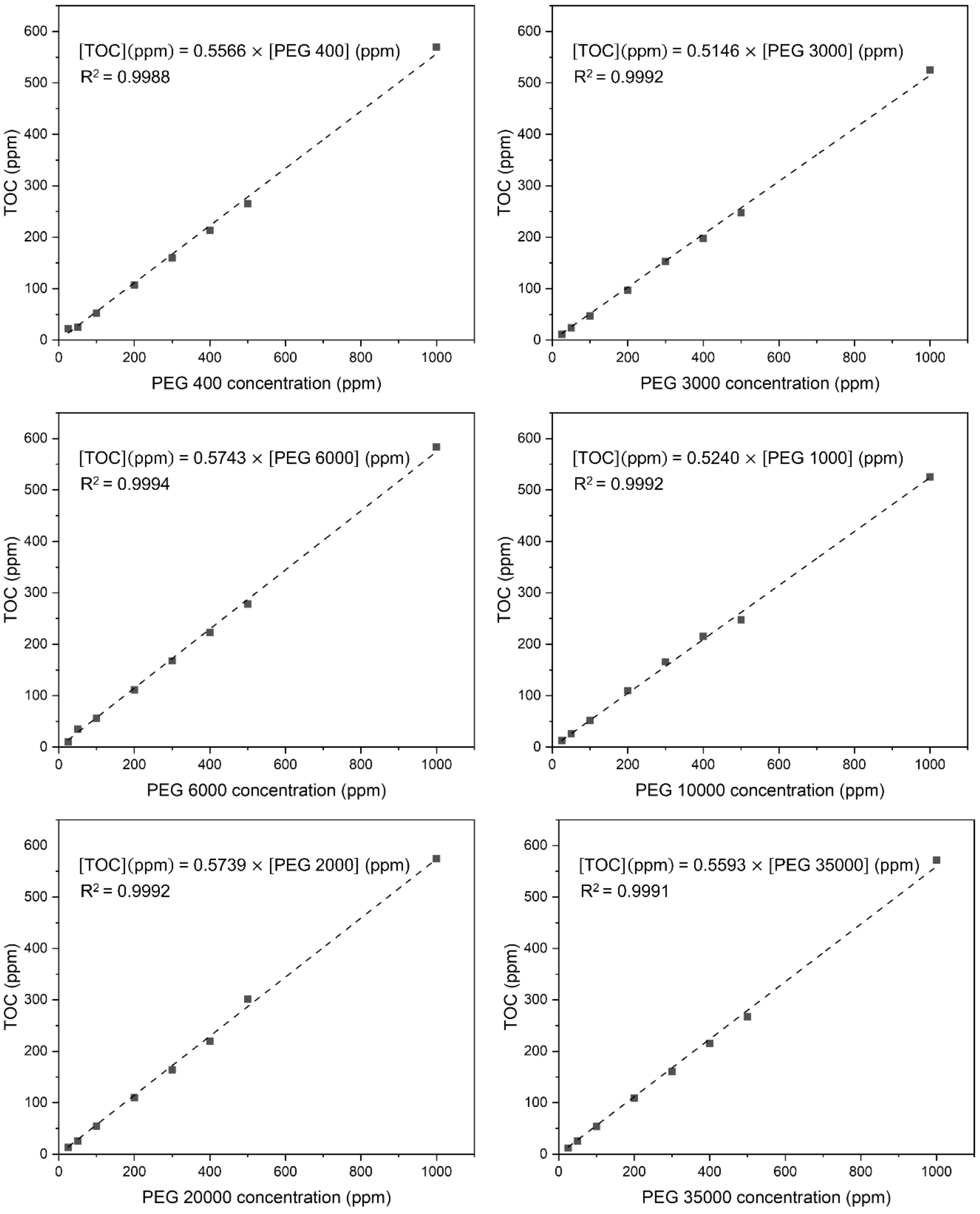

Figure B-1. Total organic carbon concentration (ppm), as a function of known concentrations (ppm) of PEG aqueous solutions. The equations are the result of a linear fit to the data, with the respective coefficient of correlation (R^2).

Appendix C. Uremic toxins calibration curves

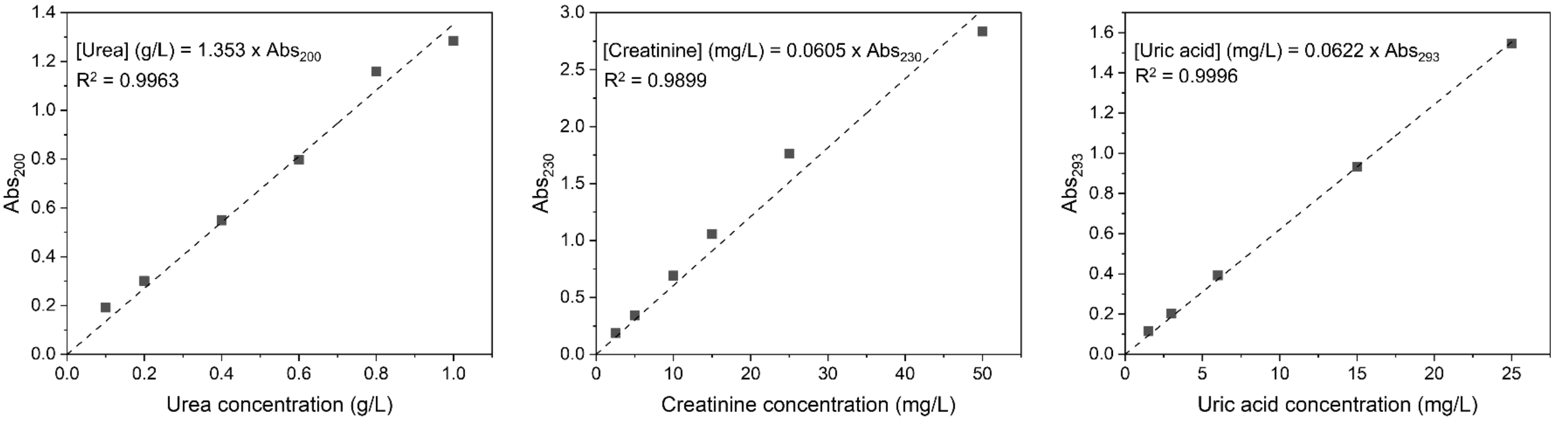

Figure C-1. Absorbance as a function of the concentration of three different toxin solutions. Measurements of absorbance were made at 200, 230 and 293 nm in the case of urea, creatinine, and uric acid, respectively. The equations are the result of a linear fit to the data, with the respective coefficient of correlation (R^2).

Appendix D. BSA calibration curves

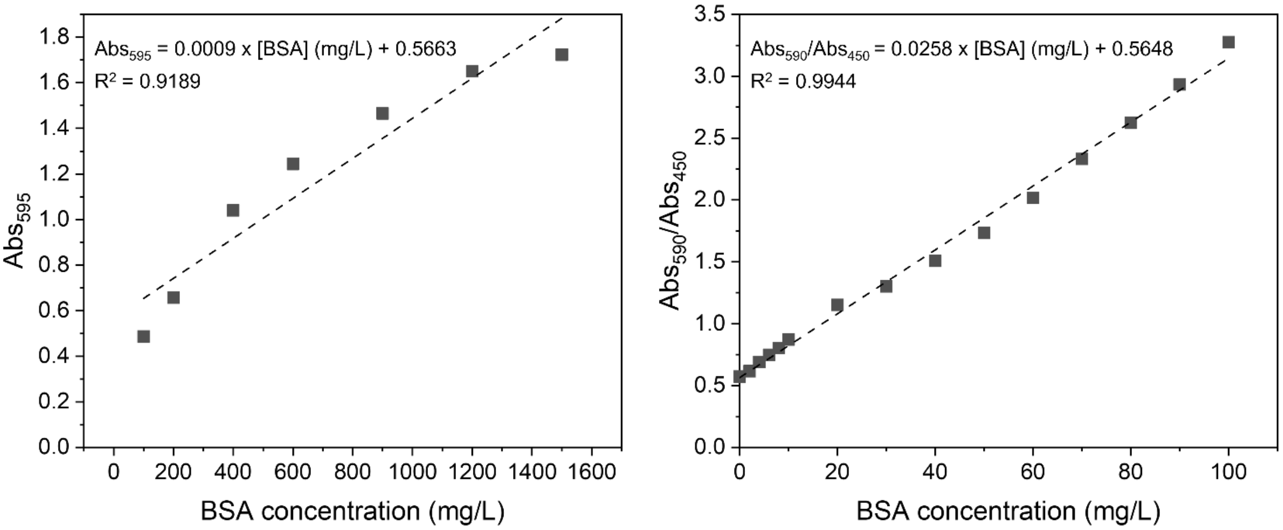

Figure D-1. Absorbance as a function of the BSA concentration. Measurements of absorbance were made at 595 nm, considering the Bradford assay (left), and simultaneously at 590 and 450 nm, considering the modified Bradford assay (right). The equations are the result of a linear fit to the data, with the respective coefficient of correlation (R^2).